3D-Printed Four-Bar Linkage Knee Prosthetic for Developing Countries

Mentor: Dr. Nidal Alif

Team 1

Joa Chi Lang, Christopher

Holowczak, Faith

Garino, Gia

Santiago, Lianis

Mendoza, Victor

Contents

Abstract

This project addresses the challenge of designing a knee replacement for above-the-knee amputation patients from low-income developing countries, typically aged 40 to 60. Given the critical factors of cost, stress resistance, and mobility, the goal is to develop a design that enhances quality of life while minimizing production, transportation, and logistic expenses. While prior designs have made progress in either cost or function, many lack objective optimization and remain unaffordable or unavailable in resource-limited settings. To overcome these limitations, this work integrates a full kinematic study to ensure smooth and stable motion, along with force and stress analysis to verify load capacity under daily activities. Optimization techniques were implemented to refine geometry, reduce error, and improve structural performance, while additive manufacturing was selected for prototyping to minimize cost and enable scalable production in remote communities. Results demonstrate that the optimized knee joint achieved a total cost of $98.09, which is 22.6% more expensive, yet remains acceptable when adapters are reused. Using Differential Evolution, the model reached an RMSE of 6.560, representing a 39% improvement over Genetic Algorithms. The design maintained a minimum safety factor of 1.2472, satisfying ISO 10328 requirements for heel contact and push-off. The joint provided 93.37° of flexion, meeting the typical 90–100° sitting range, and its final weight of 786 g, 106 g heavier than the Remotion knee but still lighter than other knees found on the market. These outcomes validate the feasibility of a low-cost, functional prosthetic knee suitable for underserved communities.

1. Introduction

A large portion of the world's population lives with some form of disability. Today, that number is estimated at 1.3 billion people, or about 16 percent of everyone on the planet, and around 80 percent of them live in low- and middle-income countries [1]. In these regions, about 8.8 million people have undergone an amputation, spanning areas such as Andean Latin America, the Caribbean, Central Asia, Sub Saharan Africa, East Asia, North Africa and the Middle East, South and Southeast Asia, and Latin America [2]. From this group, nearly 4.0 million individuals have lower limb amputations, making up almost half of all amputees in developing countries. As shown in Figure 1, disability appears more common in developed countries, which is likely due to underdiagnosis and underreporting in places with fewer medical and reporting resources.
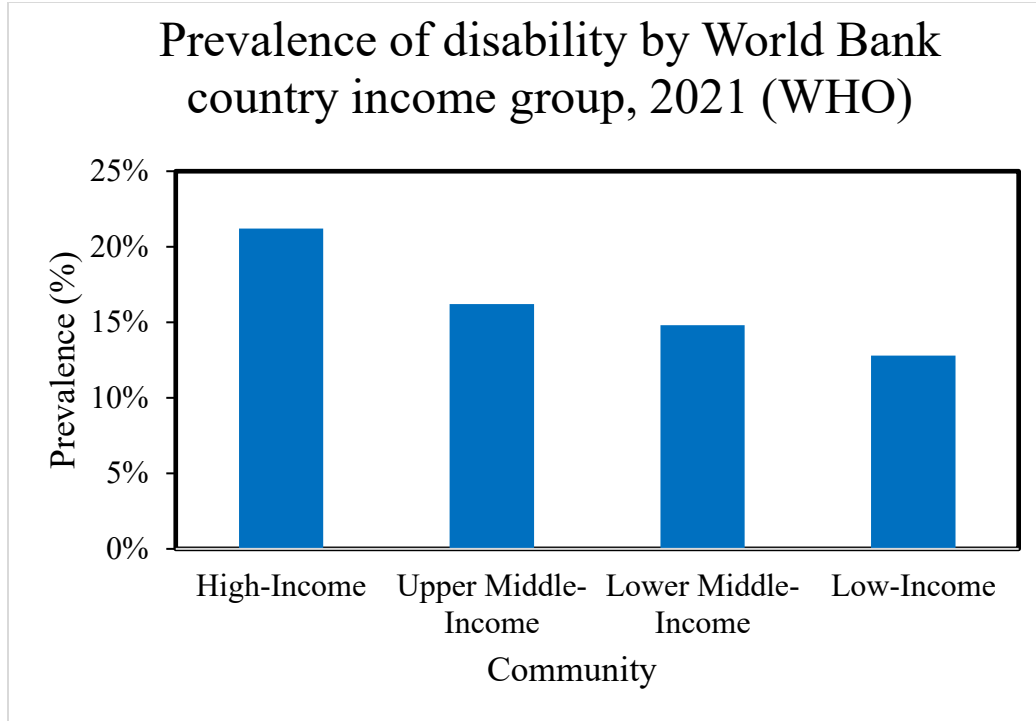
Figure 1. Prevalence of Individuals with Disability by Region (WHO, 2021) [1]

This data highlights a lack of resources for patients with disabilities. A 2006 University of Strathclyde Engineering report identified financial limitations and a shortage of trained personnel in developing countries as key barriers [3]. Even when equipment is donated, proper operation and maintenance are often lacking. Furthermore, prosthetic devices tend to have a short lifetime and low durability in extreme environmental conditions such as rugged terrain and wet weather. Similarly, costs also represent a major challenge: hospitalization can reach $120, while prosthetics imported from developed countries range from $125 to $1875. Healthcare for landmine patients, the leading cause of amputations in developing countries in 2006, has reached $3000 to $4000 [3]. These findings demonstrate the urgent need for a reliable, smooth-functioning, low-cost knee prosthetic capable of performing daily and heavy-duty activities, while being easy to maintain and widely available.

This project aims to bridge that gap by designing a low-cost, durable, and functional knee replacement tailored to above-the-knee amputees aged 40–60 living in underserved communities. The primary focus lies on affordability, durability, and mobility, utilizing advanced manufacturing techniques such as Fused Deposition Modeling (FDM) 3D printing. An optimization model for the design of the knee will be applied to create an innovative solution that enhances accessibility and

performance at low production cost. The development process includes kinematic studies to ensure smooth and natural motion, force analysis for structural optimization, and Finite Element Analysis (FEA) to validate durability under real-world conditions. Stakeholder feedback from healthcare professionals and prosthetists will guide improvements to ensure a user-centered design. Similarly, collaboration with experts in mechanical, biomedical, and materials engineering will support material selection, boundary condition definition, and computational modeling. Faculty advisors at FIU will provide guidance in mathematical modeling, optimization model, and 3D printing techniques to refine functionality and manufacturability.

Primarily, a structured design approach focused on kinematic optimization, stress validation, and iterative testing will lead to a reliable prosthetic knee. By integrating engineering expertise, computational modeling, and user feedback, this project seeks to create a practical and affordable solution that enhances the quality of life for above-the-knee amputees. The initiative also addresses broader healthcare equity issues by providing effective, accessible, and low-cost prosthetic option for underserved communities.

1.1. Problem definition and design requirements

The methodology adopted for this project follows a Model-Based Systems Engineering (MBSE) framework that integrates research, stakeholder input, computational modeling, and experimental validation [4], [5]. This approach combines both quantitative and qualitative methods, beginning with a comprehensive literature and market review to identify existing challenges, followed by data-driven material and design selection, optimization modeling, and ultimately finite element simulation and prototyping through additive manufacturing. This systematic process addresses a clear technological and accessibility gap in current prosthetic knee designs, as illustrated in Figure 2.
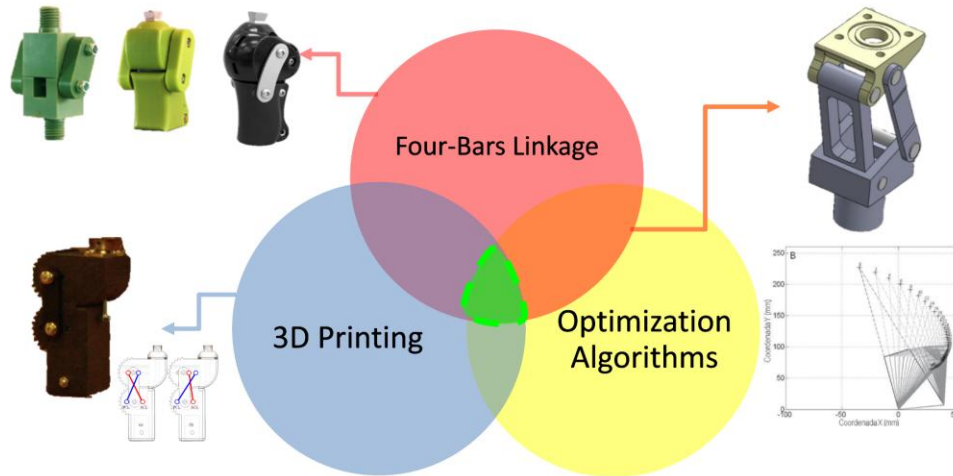
Figure 2: Conceptual relationship between the four-bar linkage design, optimization algorithms, and 3D printing used in the prosthetic knee development.

Similarly, Figure 3 shows the overall workflow used in this project. The Model Based Systems Engineering framework links four models: kinematics, mechanics, manufacturing, and standards. Together they define motion, analyze stress, assess printability, and ensure compliance with ISO 10328. Their interaction allows continuous refinement, leading to a reliable and manufacturable prosthetic knee design.
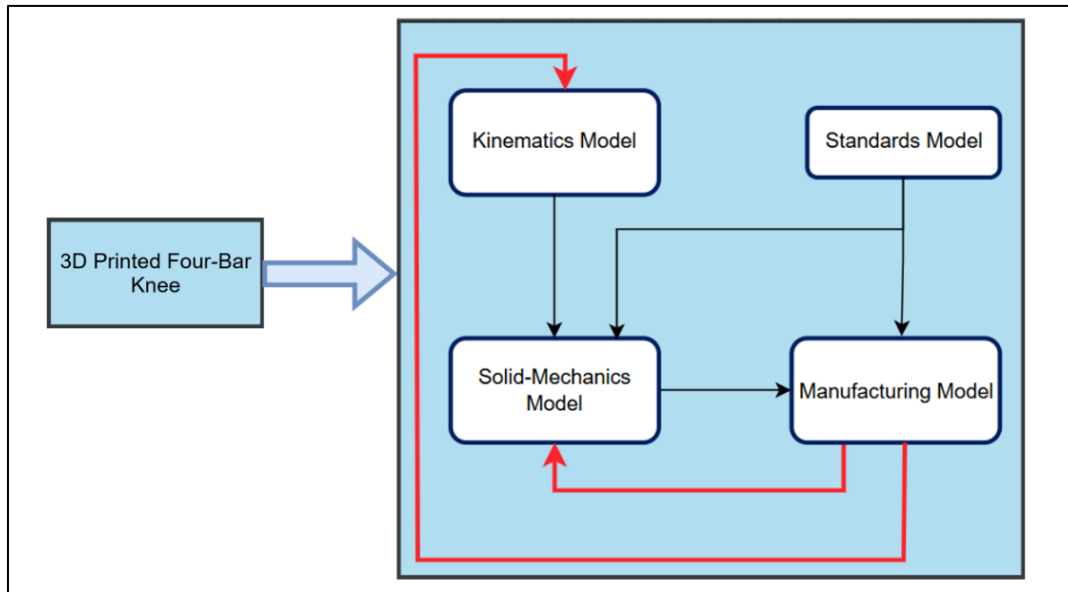

Figure 3: Workflow showing the interaction between kinematics, mechanics, manufacturing, and standards models in the prosthetic knee design.

The growing number of limb amputations in developing countries highlights an urgent need for prosthetic knees that are affordable, durable, and easy to manufacture. Many existing

designs are created for high-income users and depend on costly manufacturing processes, which makes them inaccessible to most above-the-knee amputees aged 40–60 living in low-resource regions [5]. To address this challenge, the problem was analyzed through three main dimensions: (1) design constraints defined by ISO 10328 load and fatigue standards [6], (2) computational modeling through FEA and optimization algorithms to ensure reliable motion and strength [7], and (3) manufacturing considerations focused on reducing cost, selecting suitable materials, and improving scalability [8]. These focus areas guided the development of a four-bar linkage knee mechanism designed to replicate the natural motion of the human knee while remaining lightweight, strong, and cost-effective.

A detailed market and literature survey was conducted to evaluate existing prosthetic knee designs and manufacturing methods. Comparative analysis of the ReMotion, ICRC, and Ottobock polycentric knees revealed that while polycentric mechanisms enhance gait stability and motion control, their fabrication often depends on specialized equipment and high-precision manufacturing processes, which significantly increase cost and limit accessibility in low-resource settings. For instance, the ReMotion Knee has a competitive $80 unit cost [9] but relies on injection-molded polymers that are not locally manufacturable [10]. Studies from Universidad Simón Bolívar [11] and other research on four-bar mechanism optimization [12] introduced methods such as Genetic Algorithms and Differential Evolution for dimensional synthesis, improving gait stability but remaining limited by metallic component use and high-cost CNC fabrication.

The state-of-the-art analysis considered the static, fatigue, and impact testing criteria defined by the ISO 10328 standard for lower-limb prostheses [13], which were also applied in Manodritto's study of the ICRC knee design [10]. These standards were used to evaluate mechanical performance and ensure that the proposed design meets established safety requirements. By comparing existing prosthetic knees in terms of flexion range, weight, and cost, a baseline for design success was established. Commercial microprocessor-controlled knees such as the Ottobock C-Leg and Orion3 offer advanced motion control, but their high cost (over $5,000) and heavy weight (more than 1 kg) make them unsuitable for the target population [14]. In contrast, mechanical polycentric knees like the ReMotion Knee [9] and the ICRC Knee [11] are more affordable but offer limited flexion, around 115°, and have a shorter operational lifespan.

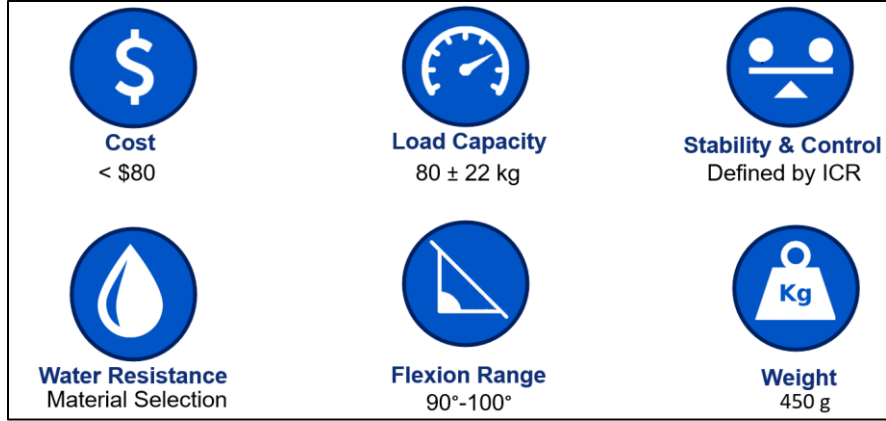To define success, measurable engineering targets were established:

Figure 4: Project design metrics.

These criteria shown in figure 4 established the main design targets that guided the project's direction. Achieving them required carefully balancing several trade-offs, such as reducing cost without sacrificing load capacity, minimizing weight while maintaining durability, and maximizing flexion without overstressing the polymer components. Ultimately, the priorities were ranked in order of importance: (1) affordability and accessibility, (2) mechanical stability and strength, (3) flexion and user comfort, and (4) environmental durability. These priorities help ensure that the prosthetic design is not only technically reliable but also practical and affordable for real-world use, setting the foundation for all the modeling, material testing, and optimization that follows.

2. Methodology
2.1. Kinematic Study

The four-bar linkage is a fundamental mechanism in prosthetic knee design due to its ability to replicate natural human knee motion. A mechanism composed of rigid bodies connected through lower pairs is known as a linkage [15]. The four-bar mechanism consists of four members, three moving links and one fixed link - connected by four pin joints. Unlike systems with a fixed axis of rotation, this mechanism rotates around a moving point known as the Instantaneous Center of Rotation (ICR), defined by the intersection of the posterior and anterior link lines, as shown in Figure 5. Studies have shown that the ICR position determines stability and control, making it essential in polycentric prosthetic designs [16].
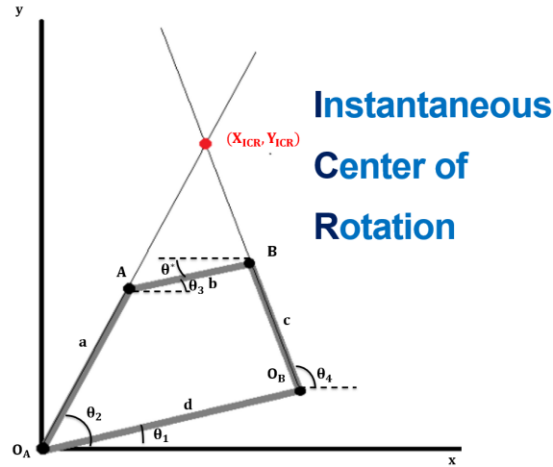
8

Figure 5: Instantaneous Center of Rotation (ICR) of Four-Bar Mechanism

The primary motion of the human knee involves flexion and extension within the sagittal plane, though it is not purely rotational. The femur slides along the tibial plateaus, shifting the rotation axis and preventing luxation, as shown in Figure 5 [17]. Prosthetic knees must replicate this motion to achieve smooth gait and stability.
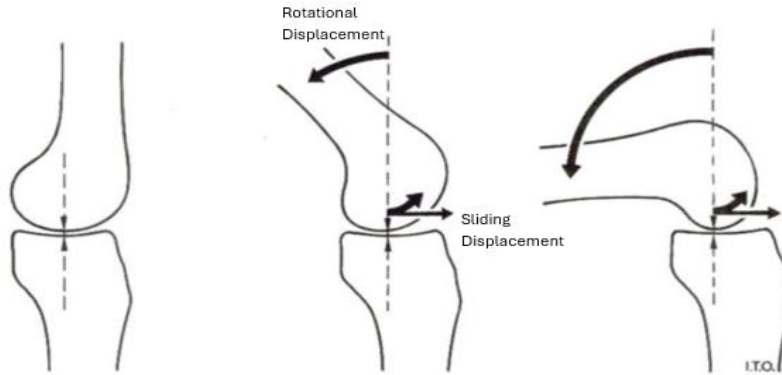

Figure 6: Flexion Extension Motion of the Knee

To replicate this motion, prosthetic mechanisms are typically monocentric or polycentric. In monocentric designs, motion occurs around a single fixed axis, requiring the user to exert higher hip moments for stability. In contrast, a polycentric knee features a moving joint axis that shifts depending on the angle of flexion-extension allowing the simultaneous translational and rotational motion through the dynamic ICR [18]. Radcliffe [16] demonstrated that the Spectrum Four-Bar Knee reduced the required hip flexion moment by 80% compared to single-axis knees.

9

Additionally, four-bar knees improve toe clearance by 0.9–3.2 cm during swing, reducing tripping risk [19]. For this reason, a polycentric design was selected for this project.

2.2. Equations and Boundary Conditions.

2.2.1. Grashoff's Rule

The Grashoff condition establishes the fundamental criterion for determining whether a linkage will exhibit full rotation or limited oscillation. By applying this condition, we ensure that the mechanism allows smooth and unrestricted movement.

$$S + L < A + B$$

Where:

S=smallest bar's length   L=Largest bar's length   A, B=other two bars' length

However, this equation can be simplified as:

$$2(S + L) < Total\ length \ldots \ldots \ldots \ldots \ldots \ldots (1)$$

2.2.2. Type of Knee

To determine the preliminary geometry that best balances control and stability for K2–K3 patients, three types of four-bar knee mechanisms were analyzed: Elevated ICR, Hyper-Stabilized, and Voluntary Control designs. Each configuration offers distinct kinematic characteristics that influence stability at heel contact and the ability to initiate knee flexion during push-off [20]. By comparing their geometric arrangements and biomechanical behavior (See Figure 7), it was aimed to identify the design that provides optimal performance for users with moderate mobility and sufficient hip control (K2-K3 patients).
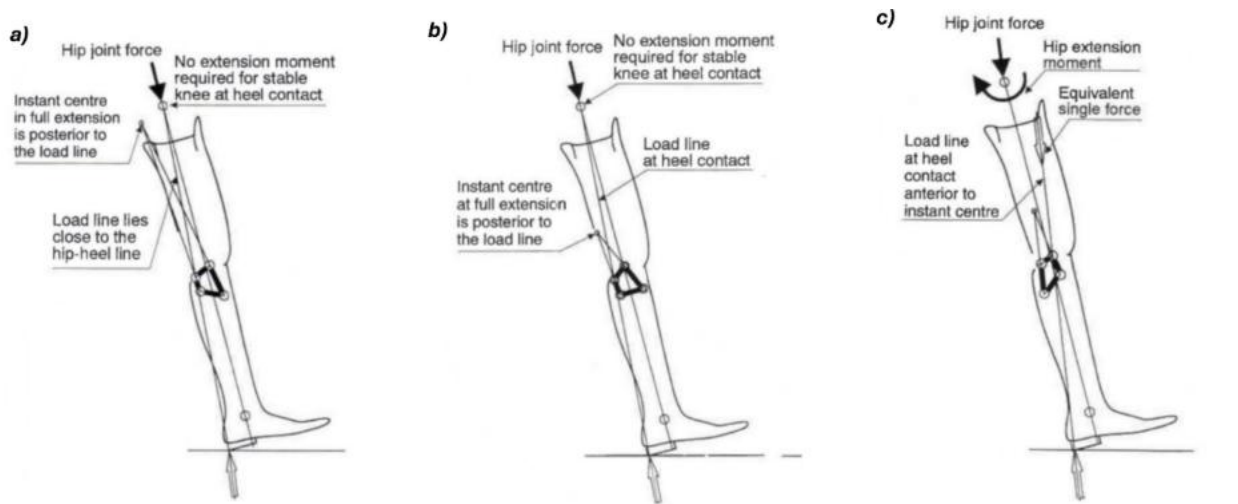

Figure 7. Types of Knees: a) Elevated ICR Knee, b) Hyper-Stabilized Knee, c) Voluntary control

Moreover, the Elevated ICR design provides strong stability at heel contact with minimal hip effort and allows easy flexion at push-off, though rapid ICR descent can reduce control during unexpected flexion. In addition, the Hyper-Stabilized Knee places the ICR far behind the load line, locking the stance for maximum stability but restricting flexion, making it suitable for low-activity users. The Voluntary Control knee maintains a moderately elevated ICR within a stable zone during early flexion, offering active amputees improved control and balance on uneven ground, slopes, and stairs.

Table 1 compares three knee mechanisms to determine the most suitable bar dimensions for the polycentric knee design, focusing on stability during Heel Contact and Push Off, which represent the extension and flexion phases of gait. For K2/K3 users, who maintain partial mobility and can produce the necessary hip moment, the goal was to balance stability and voluntary control. Equal importance was given to stability in both gait phases (0.3 each), while greater weight (0.4) was assigned to control to address the need for improved adaptability on uneven terrain common in developing regions.

Table 1: Types of Knees Decision Matrix

Type	Stability at Heel Contact	Stability at Push Off	Control at Push Off	Total
Weight	0.30	0.30	0.40	1.00
Elevated ICR	1.00/1.00	1.00/1.00	0.00/1.00	0.60
Hyper-Stabilized	1.00/1.00	1.00/1.00	0.00/1.00	0.60
Voluntary Control	0.50/1.00	0.50/1.00	1.00/1.00	0.70

By choosing the Voluntary Control Knee, it was defined that the anterior bar (a) must be longer than the posterior bar (c) as shown in figure 1:

$$c < a \ldots \ldots \ldots (2)$$

2.2.3. Gait Analysis Data

To have the Force Reaction Forces (FRPs) at heel contact and Push-Off to evaluate the stability of the knee by checking the location of the ICR with respect to the load line, data shown in Figure 4 from [18] was used considering the following dimensions and rotations for the leg:

Table 2: Dimensions and Rotations of the Testing Leg from [18]

Parameter	Heel Contact	Push Off
System Rotation	17.35° CCW from +y-axis	26.56° CW from +y-axis
Thigh (mm)	(−150, +310) from knee center	(+60, +320) from knee center
Calf (mm)	(+130, −350) from knee center	(−130, −360) from knee center
Force Point (mm)	(+50, −380) from knee center	(−40, −370) from knee center
Force Angle (°)	66.80° from +x-axis	87.455° from +x-axis

These parameters are needed because the distances between the ICR, when the leg is fully extended, and the force point from the FRP determines knee stability by defining the hip moment required from the amputee during the extension and swing phases (Eq 3).

$$M_h = PL \left(\frac{x}{y}\right) \ldots \ldots \ldots \ldots \ldots (3)$$
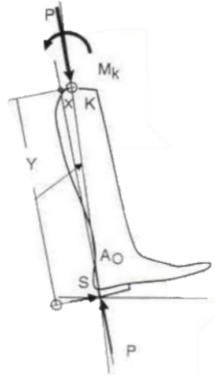

Figure 8: Illustration of Parameters for Hip Moment Equation

As shown in Figure 8, P and L are constant, while x and y represent the distances from the ICR to the load line and point of contact. A negative x/y ratio at heel contact indicates self-stability without hip effort, while a positive ratio requires slight hip extension. Radcliffe [20] found that the Hosmer Spectrum Knee maintains a smooth ICR path and meets this stability condition, improving control and balance during walking and making it an effective model for the desired trajectory.

2.2.4. Equations of ICR Motion

To calculate the different locations of the ICR, the following equations from [18] were used. These governing equations are derived by using the loop enclosure rule that takes the four-bar linkage as a chain of vectors that starts at O_A and ends at the same point (Figure 1).

Loop − Closure Equations:

$$x: a\cos\theta_2 + b\cos\theta_3 - c\cos\theta_4 - d\cos\theta_1 = 0$$

$$y: a\sin\theta_2 + b\sin\theta_3 - c\sin\theta_4 - d\sin\theta_1 = 0$$

After some algebra and trigonometry, the θ_2 and θ_4 are got as functions of the lengths of the four bars and the design angles of the top and bottom bars:

$$\theta_2 = 2\tan^{-1}\left(\frac{-B \pm \sqrt{B^2 - 4AC}}{2A}\right) = f_1(a, b, c, d, \theta_1, \theta_3) \dots\dots\dots\dots\dots (4)$$

$$\theta_4 = 2\tan^{-1}\left(\frac{-E \pm \sqrt{E^2 - 4DF}}{2D}\right) = f_2(a, b, c, d, \theta_1, \theta_3) \dots\dots\dots\dots\dots (5)$$

Where:

$$\theta_3 = \theta^* + \theta_R \dots\dots\dots (6)$$

$$A = \frac{(a^2 + b^2 - c^2 + d^2)}{2ab} - \frac{d(\cos\theta_1\cos\theta_3 + \sin\theta_1\sin\theta_3)}{a} - \cos\theta_3 + \frac{d}{b}\cos\theta_1 \dots\dots\dots (7)$$

$$B = 2\left(sin\theta_3 - \frac{d}{b}sin\theta_1\right) \dots\dots\dots\dots\dots (8)$$

$$C = \frac{(a^2 + b^2 - c^2 + d^2)}{2ab} - \frac{d(\cos\theta_1\cos\theta_3 + \sin\theta_1\sin\theta_3)}{a} + \cos\theta_3 - \frac{d}{b}\cos\theta_1 \dots\dots\dots (9)$$

$$D = \frac{(b^2 - a^2 + c^2 + d^2)}{2bc} - \frac{d(\cos\theta_1\cos\theta_3 + \sin\theta_1\sin\theta_3)}{c} + \cos\theta_3 - \frac{d}{b}\cos\theta_1 \dots\dots\dots (10)$$

$$E = 2\left(\frac{d}{b}sin\theta_1 - sin\theta_3\right) \dots\dots\dots (11)$$

$$F = \frac{(b^2 - a^2 + c^2 + d^2)}{2bc} - \frac{d(\cos\theta_1\cos\theta_3 + \sin\theta_1\sin\theta_3)}{c} - \cos\theta_3 + \frac{d}{b}\cos\theta_1 \dots\dots\dots (12)$$

As observed in Eq. 4, Eq. 5, Eq. 13, and Eq. 14, this makes the design problem a multi-objective due to the dependence on design parameters of the mechanism and the boundary conditions previously defined.

$$X_{ICR} = \frac{X_{O_B}\tan\theta_4 - Y_{O_B}}{\tan\theta_4 - \tan\theta_2} - d\cos\theta_1 - X_{O_B} = f_3(a, b, c, d, \theta_1, \theta_2, \theta_R, \theta^*) \dots\dots\dots (13)$$

$$Y_{ICR} = \frac{(X_{O_B}\tan\theta_4 - Y_{O_B})\tan\theta_2}{\tan\theta_4 - \tan\theta_2} - d\sin\theta_1 + Y_{OB} = f_4(a, b, c, d, \theta_1, \theta_2, \theta_R, \theta^*) \dots \dots (14)$$

2.2.5. Optimization Algorithm Selection and Implementation

Several optimization algorithms have been applied to improve four-bar mechanism performance, generally classified as analytical or numerical. Numerical methods include deterministic and heuristic approaches; the latter are slower but more robust for global, multi-objective optimization [21]. To identify the most suitable algorithm, four common techniques were compared based on popularity, research interest, and reported error (Table 3). From this analysis, Differential Evolution (DE) was selected as the most effective and reliable method.

Table 3: Optimization Methods Decision Matrix [21] [22]

Algorithm	Popularity	Interest Trend	Error	Total
Weight	0.10	0.40	0.50	1.00
Particle Swarm Algorithm	75000+ citations (1.00)	2.00/3.00 (0.67)	5.55 (0.84)	0.79
Genetic Algorithm	70000 citations (0.93)	1.00/3.00 (0.33)	10.1 (0.46)	0.46
Differential Evolution	**30000 citations (0.40)**	**3.00/3.00 (1.00)**	**5.52 (0.84)**	**0.86**
Simulated Annealing	15000 citations (0.20)	2.00/3.00 (0.67)	4.65 (1.00)	0.79

The DE algorithm works by iteratively generating new candidate solutions through scaled vector differences between population members (Figure 9b). Each cycle begins with Initialization, defining boundaries and control parameters, followed by Differential Mutation, where a mutation factor (M) determines variation amplitude. Crossover, controlled by the crossover rate (CR), blends mutated and non-mutated individuals to maintain diversity (Figure 9c). Finally, Selection applies a greedy criterion to retain candidates with the best fitness.
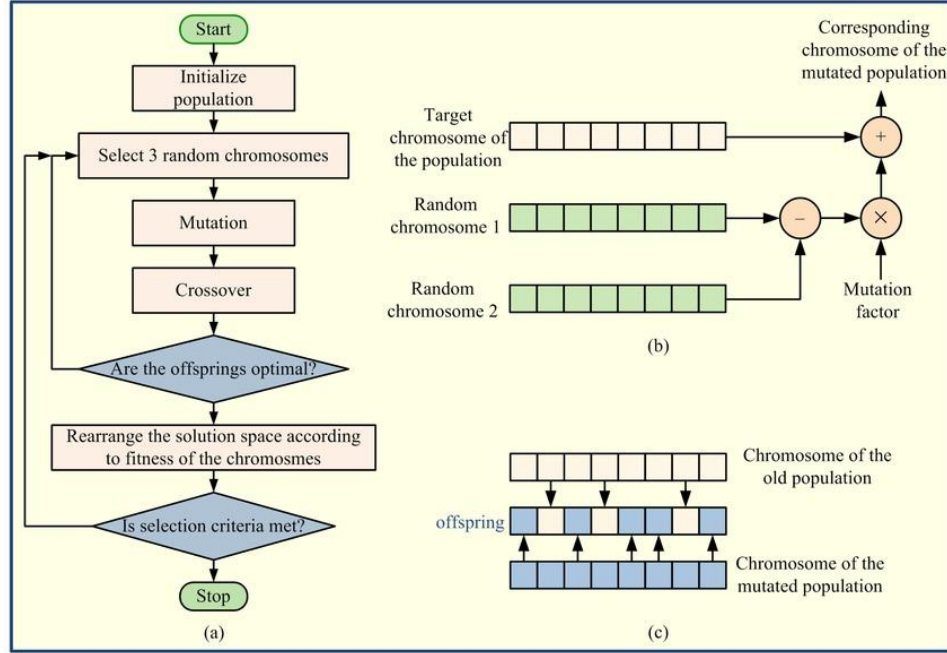
Figure 9: (a) DE Flowchart, (b) Mutation Process, (c) Crossover Process

For this study, each candidate solution was represented by six design variables corresponding to prosthetic knee dimensions provided by Hanger Clinic. The DE algorithm ran with 300 individuals and 1500 generations, ensuring a balance between exploration and convergence. The parameters used are shown in Table 4.

Table 4: Control Parameters

Parameter	Value
No. of Individuals	300
Max. Generation	1500
a_{range} (mm)	[20, 50]
b_{range} (mm)	[20, 60]
c_{range} (mm)	[20, 50]
d_{range} (mm)	[20, 50]
$\theta_{1_{range}}$ (°)	[0, 45]
θ^*_{range} (°)	[0, 35]
M	0.5
CR	0.5
F	0.8

The fitness function (Figure 10) used a greedy selection process based on the Root Mean Squared Error (RMSE) between the desired Instantaneous Center of Rotation (ICR) trajectory

15

from the Hosmer Spectrum Knee and the simulated one. The algorithm iterated until convergence, producing an optimized configuration that closely replicated natural knee motion.
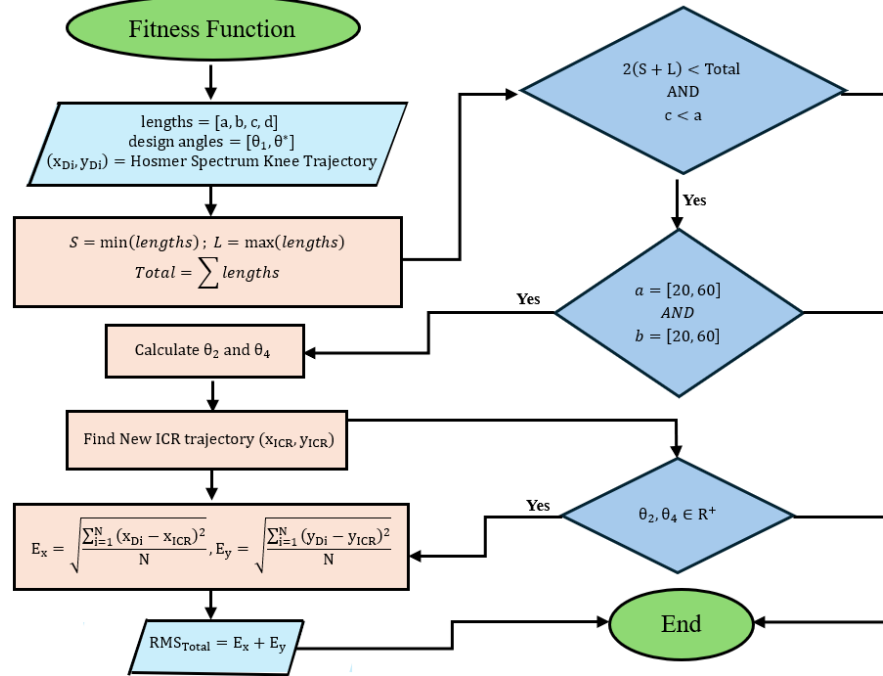

Figure 10: Proposed Fitness Function for Kinematic Study

2.3. Material Selection

Selecting the right materials was essential to develop a prosthetic knee that is affordable, durable, and suitable for low-resource environments. Both quantitative factors (cost, density, stiffness, strength) and qualitative ones (printability, corrosion resistance, water durability) were considered using a weighted decision matrix. Cost and density were minimized to improve comfort, while stiffness, strength, and water resistance were prioritized for long-term reliability.

Common 3D printing materials such as PLA, PETG, Nylon Carbon Fiber, and PLA Plus were analyzed (Table 5). PLA is the most affordable and widely available, making it ideal for accessibility, though it weakens in humid environments [23]. PETG improves durability and moisture resistance but increases cost and print complexity [24]. Nylon Carbon Fiber offers superior strength and stiffness but remains expensive and less practical for rapid local production [25]. PLA Plus, a tougher PLA variant, provides a good compromise between printability, strength, and environmental resistance [26].

Table 5: Materials decision matrix

Material	Cost ($/kg)	Density (g/cm3)	Elastic Modulus (GPa)	Yield Strength (MPa)	Water Resistance	Total
Weight	**0.25**	**0.15**	**0.20**	**0.20**	**0.20**	**1.00**
Nylon Carbon Fiber	50-750 (0.05)	1.00 (1.00)	6.00 (1.00)	100 (1.00)	A (1.00)	0.76
PLA	**10-40 (1.00)**	**1.24 (0.81)**	**3.14 (0.52)**	**69 (0.69)**	**A (1.00)**	**0.81**
PETG	20-60 (0.67)	1.27 (0.79)	2.02 (0.34)	50 (0.50)	A (1.00)	0.65
PA-12	100-150 (0.27)	1.02 (0.98)	1.40 (0.23)	60 (0.60)	A (1.00)	0.58
PC	40-75 (0.53)	1.20 (0.83)	2.35 (0.39)	63 (0.63)	A (1.00)	0.66
ABS	10-40 *(1.00)*	1.04 (0.96)	2.65 (0.44)	52 *(0.52)*	B *(0.75)*	0.74

To complement the selected polymers, metallic materials were also evaluated for parts that experience higher loads, such as pins and connectors. Table 6 compares stainless steel, titanium, and aluminum using the same weighted criteria. Stainless steel offered the best combination of strength, cost, and corrosion resistance, making it the most practical choice for humid environments. Titanium showed excellent strength [27] but was significantly more expensive, while aluminum was lightweight yet less resistant to corrosion [28].

Table 6: Materials Decision matrix with Metallic Materials

Material	Cost ($/kg)	Density (g/cm^3)	Elastic Modulus (GPa)	Yield Strength (MPa)	Water Resistance (Galvanic Series in V)	Total w/ Water Resistance
Weight	**0.25**	**0.15**	**0.21**	**0.21**	**0.18**	**1.00**
Stainless Steel	**157 (1.00)**	**7.99 (0.34)**	**190 (1.00)**	**494 (0.50)**	**-0,1 to 0 (0.75)**	**0.75**
Titanium	495 (0.32)	4.42 (0.61)	126 (0.66)	985 (1.00)	-0.125 to 0.05 (1.00)	0.70
Aluminum	202 (0.78)	2.68 (1.00)	68 (0.36)	206 (0.21)	-1.00 to -0.75 (0.30)	0.52

Overall, PLA Plus was chosen for the main prosthetic parts because it offers a good balance between cost, strength, and ease of printing. Stainless steel was selected for the joints and connectors since it provides the durability and corrosion resistance needed for daily use. Together, these materials create a reliable, affordable, and easy-to-manufacture prosthetic knee that can withstand long-term use in developing communities.

2.4. Manufacturing Process

The process began with the selection of Fused Deposition Modeling (FDM) as the preferred additive manufacturing method. FDM was chosen due to its practicality and affordability, especially for producing complex mechanical geometries that require precise dimensional control. Unlike other additive techniques such as Selective Laser Sintering (SLS) or Stereolithography (SLA), FDM offers geometric accuracy, material accessibility, and post-processing flexibility. Based on what FDM offers, this is the best choice for iterative cycles, where design modifications are frequent, and development time is important. Given the prosthetic knee design, FDM's ability to produce continuous contours with predictable layer bonding was a decisive factor. To enhance mechanical reliability, print orientation and layer thickness were strategically optimized to reduce anisotropy. This ensured critical load-bearing regions. Especially around pivot points and screw interfaces, which were aligned with the filament deposition direction, thereby minimizing the risk of failure during mechanical testing.

Polylactic Acid Plus (PLA+) was selected as the filament material for this prototype due to its favorable mechanical and printing characteristics. PLA+ offers relatively high stiffness, excellent dimensional stability, and ease of use, making it ideal for producing accurate test components. While alternative materials such as Carbon Fiber or nylon provide greater toughness, they often necessitate heated build chambers and more complex print tuning. PLA+, on the other hand, can be printed with minimal warping and a smooth surface finish, which is particularly important for creating precisely aligned linkage interfaces. For early-stage evaluation, PLA+ allows for easy access and testing to assess motion and mechanical clearances without the interference of excessive deformation, with a low cost contribute to sustainability, enabling multiple design iterations to be produced affordably and with minimal environmental impact.
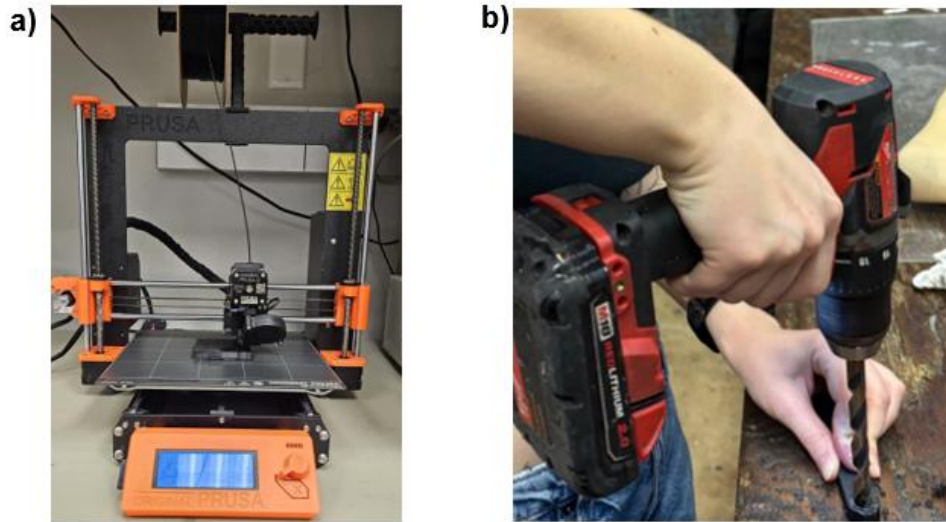
Figure 11: Manufacturing Processes a) 3D Printing using Prusa i3 MK4, b) Drilling Holes from Bars

Once the printing phase was complete, manual machining operations were carried out to prepare the mechanical joints. Specifically, four holes were drilled using a center drill creating a 6 mm hole-diameter, precisely positioned according to the geometry of the four-bar mechanism [3]. These holes were located on both the top and bottom regions of the printed knee structure, corresponding to the attachment points for the male pyramid adaptors. Manual drilling was chosen over a CNC machine to provide tactile control and avoid localized heating that could compromise the integrity of the PLA material. Utilizing moderate spindle speeds and slow feed rates were employed to maintain clean, circular edges and prevent delamination around the hole walls. A hand-held power drill, in figure 11 was used for post-processing on the holes of the link to create a cleaner tolerance measurement of 10.2mm to safely fit the 10mm diameter shoulder screws into our prototype 1. Following the drilling process, each hole on the top and base was threaded using an M6 tap to create robust and repeatable fastening points. Manual threading allowed for precise control over thread depth and engagement, reducing the likelihood of cracking or stripping the thermoplastic material. This step was critical to ensure the mechanical reliability of the assembled prosthetic knee.
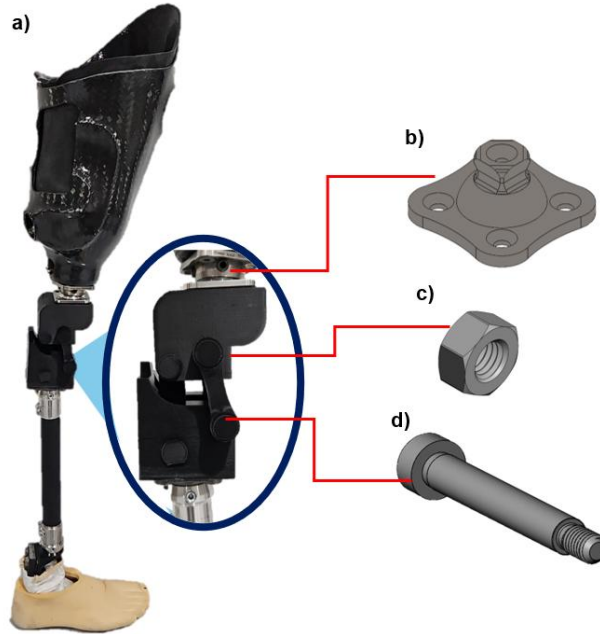
Figure 12: a) Final Physical Assembly, b) Pyramid Adapter, c) M8 Hex Nut, d) M8 Shoulder Screw

Next, male pyramid adaptors were chosen for both the upper and lower sections of the printed knee joint, as shown in figure 12. The pyramids are attached using eight standard flat-top M6 screws, each measuring 25 mm in length. These adaptors serve as essential components in modular prosthetic systems, providing the mechanical interface between the knee unit and the prosthetic socket and pylon [29]. The M6 screws offered sufficient thread engagement strength for the PLA substrate while maintaining a compact connection profile while fitting in with the standards. Flat-top screws were selected to ensure flush contact with the adaptor surface, promoting even clamping pressure and minimizing rotational play.

The final assembly utilized four 18-8 stainless-steel shoulder screws [30], each selected in prototype-specific lengths: four pins measuring 35.25 mm with a 12.6 mm diameter, the back pin on the central bar measuring 61.5 mm with a 12.6 mm diameter, and the bottom pin measuring 61.5 mm with a 15.75 mm diameter. These shoulder screws functioned as rotational pivots within the four-bar mechanism, enabling each segment to move relative to the others with precise spacing and minimal friction.

Stainless steel was chosen for the high Young's modulus, which provides excellent stiffness and resistance to elastic deformation underload [30]. Compared to other commonly used

metals, stainless steel exhibits a relatively high Young's modulus and provides strong resistance to environmental corrosion [30]. This property is vital for maintaining consistent kinematic performance in a prosthetic joint, where even minor deflections can affect gait stability. To secure the shoulder screws, Standard stainless-steel M8 hex nuts were threaded onto the ends. These hex nuts lock the shoulder screws in place while providing a compact, low-profile closure that reduces sharp edges or protruding threads minimizing snagging and improving safety. Because the hex nuts are made of stainless steel, they deliver excellent corrosion resistance and durability, ensuring the joint remains secure even under repeated use, vibration, or environmental exposure [31]. When addressing excess friction, a small amount of lubricant can be applied to each pivot interface to facilitate smooth rotational motion and reduce frictional wear between the metal fasteners and PLA components. After assembly, the linkage was manually cycled to verify full range of motion and confirm the absence of misalignment or binding.

Overall, the manufacturing workflow emphasized precision, modularity, and accessibility. The use of FDM printing with PLA enabled rapid iteration of design variations, functional clearance assessments, and mechanical alignment evaluations without the need for costly metal fabrication. By combining additive manufacturing with straightforward manual machining, the process leveraged the strengths of both modern and traditional fabrication techniques. The incorporation of standardized hardware such as M6 flat-head screws, pyramid adaptors, and hex nuts to further enhanced assembly, allowing the design to be easily disassembled for inspection or modified for future testing phases.

2.5. Compression Test Data and Results

Compression testing was carried out to understand how the 3D-printed PLA material behaves under load and to obtain the yield strength values later used in the ANSYS simulation. The tests followed the ASTM D695 standard for rigid plastics. Each specimen measured 12.7 × 12.7 × 25.4 mm, as specified by the standard. A total of 18 samples were tested, divided into three infill percentages (60%, 80%, and 100%) and three print orientations (x, y, and z), with two samples tested for each condition to ensure consistent results. The parts were printed using a gyroid infill pattern, chosen because it distributes stress evenly in all directions and performs better under compression than cubic or triangular patterns. This pattern also helps minimize weak points

between layers, which is important for parts that experience repeated loading, such as prosthetic components.

Testing was done on a universal testing machine (MTS Criterion Model 43) at a loading rate of 1.3 mm/min, in accordance with ASTM D695 as shown in Figure 13 [32]. Each specimen was positioned so that the compressive force acted along the z-axis, while additional tests were performed in the x and y directions to observe how the print orientation affected performance. During each test, data for force, displacement, and time were collected to generate stress–strain curves for each infill configuration as shown in Figure 14.

Figure 13: Compression testing set up
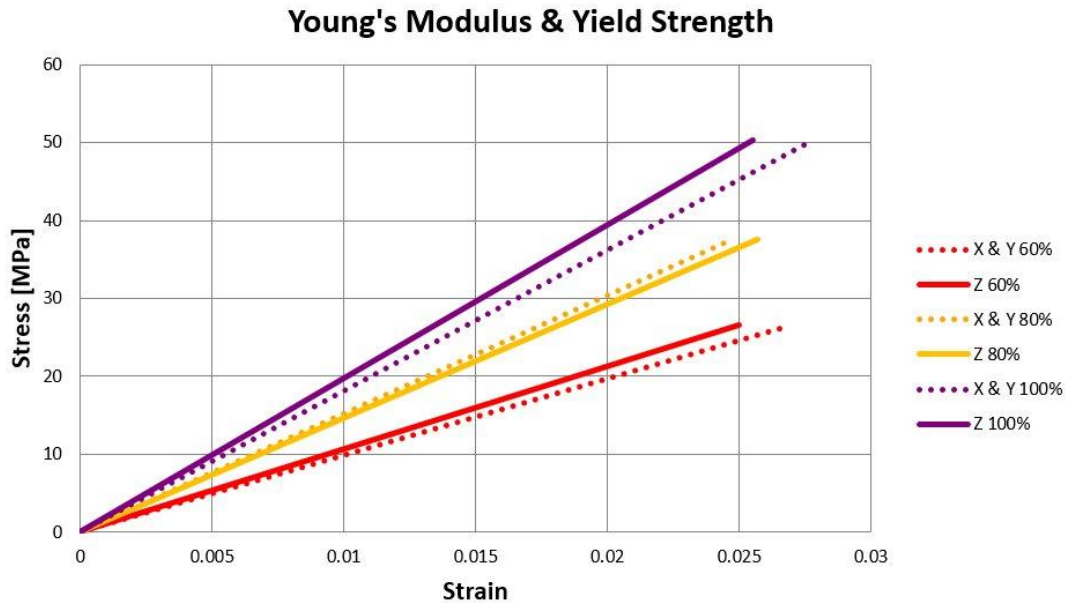
Figure14: Stress–Strain Curve for Different Infill Percentages.

The results showed that as the infill percentage increased, the material became stronger and more rigid. The 100% infill samples had the highest stiffness and yield strength, showing very little deformation before failure. At 80% infill, the samples were still strong but began to compress earlier, while 60% infill samples showed visible deformation and lower load capacity due to internal voids. These results confirmed that fully solid specimens provide the best strength-to-weight ratio for this application. The yield strength values obtained from the 100% infill samples were later used in the ANSYS structural analysis to accurately simulate how the prosthetic knee would perform under real loading conditions.

2.6. Structural Study (ANSYS)

Human gait follows a quasi-static cycle beginning and ending with heel contact of the same leg [33]. As shown in Figure 15, heel strike occurs at 0% of the cycle, the peak heel-contact reaction at 8%, and push-off at 45% [4], representing the critical loading points. Following ISO 10328, structural evaluation was performed under Condition 1 (heel contact) and Condition 2 (push-off) [34], as shown in Figure 15. These conditions were used for dimensioning the system to meet a minimum safety factor of 1.25, based on material properties of printed PLA (Section 2.5) and 18-8 stainless steel (Table 7).
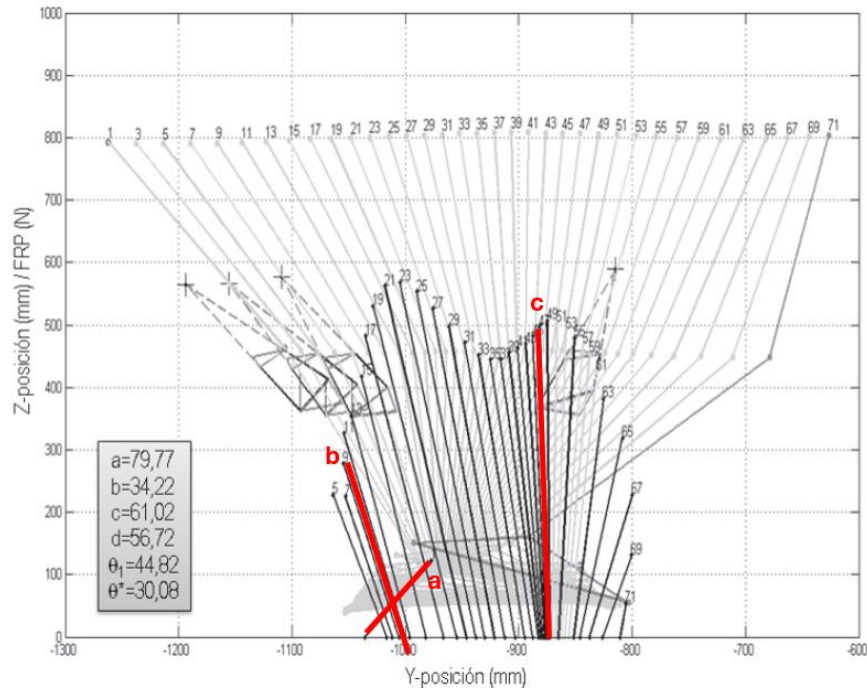
Figure 15: Gait Analysis Data with FRPs at a) initial heel contact, b) force response at heel contact, c) push off. [4]

Table 7: Mechanical Properties of Implemented Materials

Property	PLA	18-8 Stainless Steel
Young's Modulus [GPa]	2.94	193
Poisson's Ratio	0.33	0.29
Yield Strength [MPa]	50.35	207

Finite Element Analysis (FEA) in ANSYS Workbench Mechanical 2025 was used to optimize and validate the proposed design made in SolidWorks 2025 by assessing stresses and safety factors for the entire assembly and individual components under the three defined loading conditions.

2.6.1. FEA Set-Up

The simulation settings used in all analyses are summarized in Table 8.
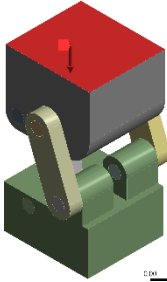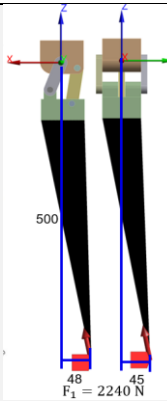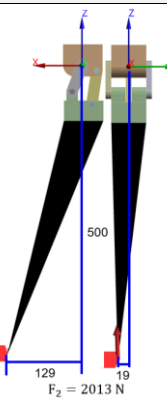
Table 8: Mesh Settings

Setting	Description/Value
Mesh method	Tetrahedral, Quadratic elements (higher accuracy); local refinement in curved features
Initial Mesh Size	5.0 mm
Final Mesh Size	1.2 mm
Zero Displacement	Pins axially constrained

Three loading conditions were analyzed: an axial compression test to confirm contacts and boundary conditions, followed by Condition 1 (heel contact) and Condition 2 (push-off) to assess structural reliability. All simulations were validated through a mesh convergence study by progressively reducing element size until solution stabilization. For the gait-related conditions, a remote force was applied to avoid explicitly modeling the pylons and reduce computational cost; the required bending and torsional moments were generated through positional offsets listed in Table 9.

Table 9: Loading Conditions

Axial Compression	• $F_x = 0$ N • $F_y = 0$ N • $F_z = -1000$ N $= F_{Total}$ • Total force distributed in top face. • Fixed support on bottom face.	
Condition 1 (Heel Contact)	• $F_x = 431.87$ N • $F_y = -410.27$ N • $F_z = 2159.3$ N • Offset force distributed in bottom face. • Fixed support on top face.	
Condition 2 (Push Off)	• $F_x = -227.47$ N • $F_y = -64.42$ N • $F_z = 1998.9$ N • Offset force distributed in bottom face. • Fixed support on top face.	

3. Results and Discussion
3.1. Kinematic Study Results

Figure 16 shows the total Root Mean Square Error (RMSE) between the best resulting ICR trajectory from each iteration as a function of generation number. The RMSE rapidly decreases within the first 200 generations and stabilizes thereafter, indicating effective convergence toward the optimal design with minimal kinematic errors.
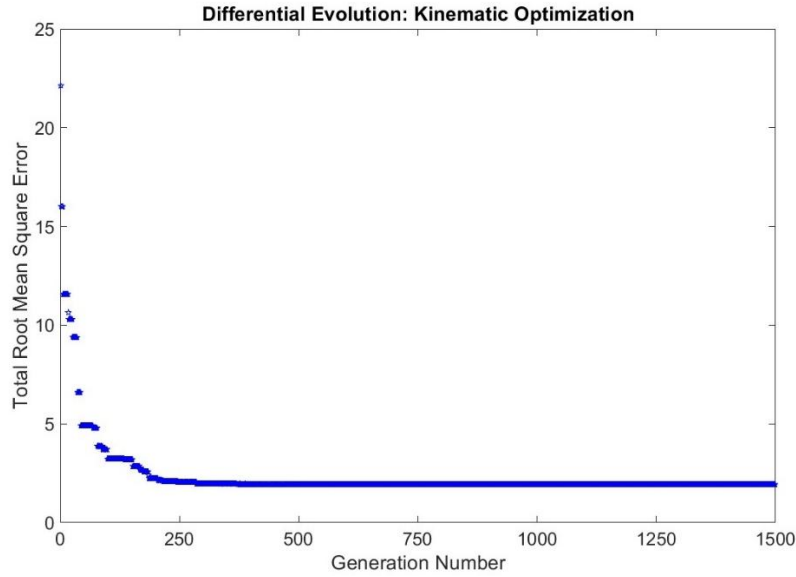
Figure 16: Convergence from Kinematic Optimization using Deferential Equation (DE)

Figure 17 complements the previous analysis by illustrating the evolution of the ICR trajectory defined by its x and y coordinates with respect to the knee center (B) as a function of the flexion angle. In early generations (i = 0–10), the simulated trajectories deviate markedly from the desired experimental data (blue curves), with RMSE values exceeding 10. As the optimization progresses (i = 19–35), the trajectories increasingly align with the target data, and the RMSE drops below 3. From generation i ≥ 40, both ICR coordinates exhibit strong agreement with the desired motion, with RMSE stabilizing around 1.93, confirming convergence of the algorithm and accurate reproduction of the desired knee kinematics.
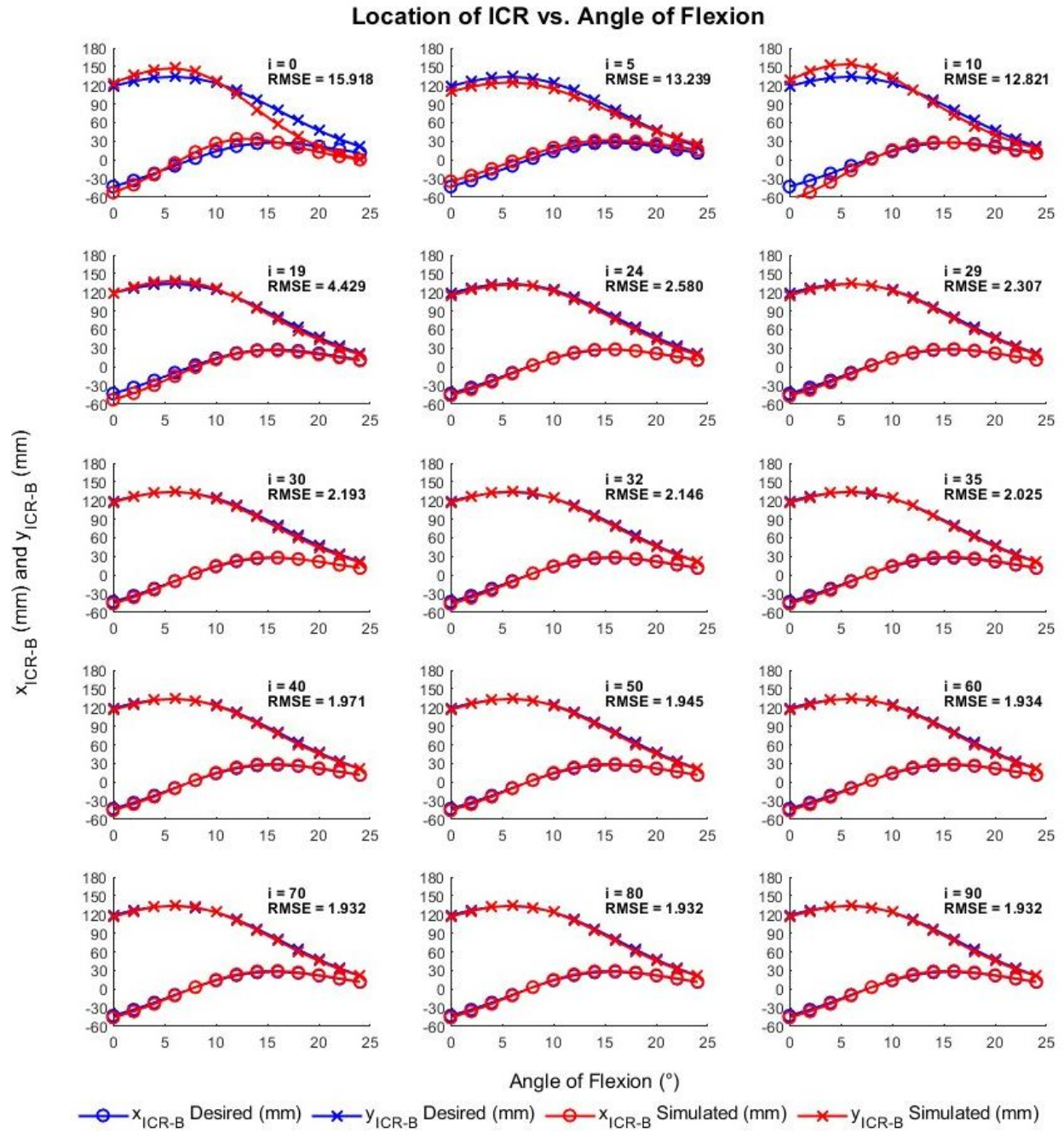
Figure 17: Evolution of Best Design using DE

To validate the performance of the proposed DE algorithm, its results were compared with those obtained using a Genetic Algorithm (GA) from prior work [18]. Figure 18 presents this comparison, demonstrating that the DE approach achieves substantially higher accuracy, with an RMSE of 6.560 compared to 10.78 for the GA—an error reduction of approximately 39.15%. The DE-optimized trajectories exhibit strong agreement with the desired Instant Center of Rotation (ICR) paths in both the *x* and *y* directions, whereas the GA results display noticeable deviation in the *x*-direction (Figure 18a). This outcome confirms that the Differential Evolution method provides superior kinematic fidelity and more effective error minimization in the optimization of the four-bar linkage mechanism.
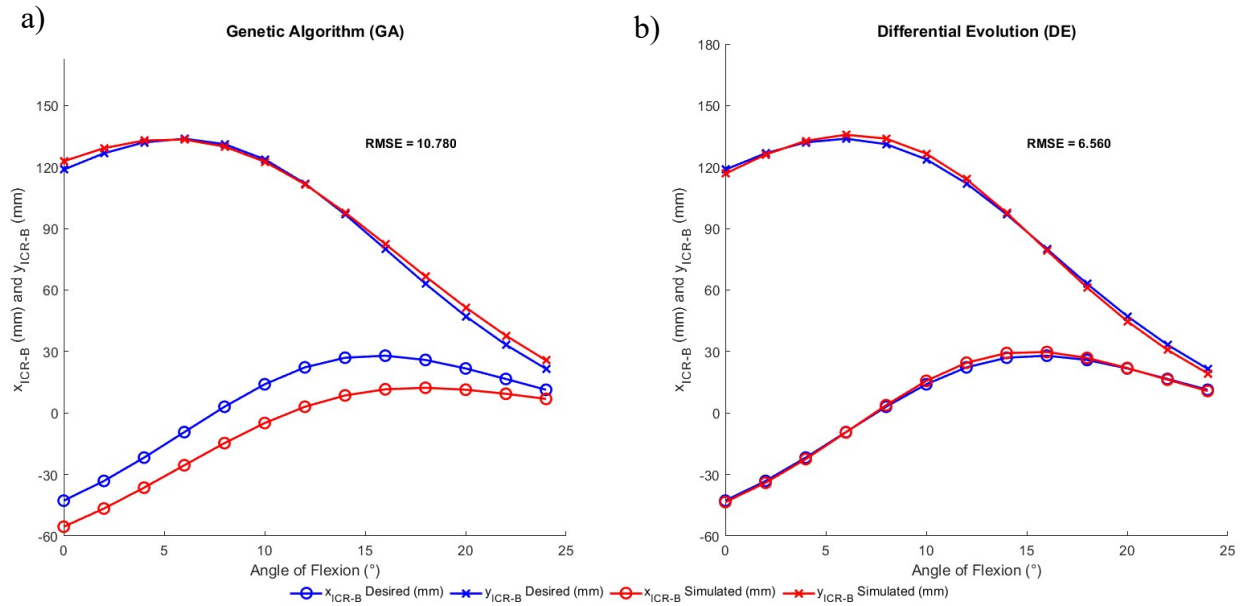
Figure 18: Performance Comparison of GA and DE

After generating the new dimensions for the prosthetic knee (Figure 19), its control and stability were evaluated based on the trajectory of the ICR. As shown in Figure 19, the ICR location did not exhibit significant displacement in the y-direction during the initial 5 degrees of flexion, with a variation of approximately 20.7 mm (2.07 cm). This indicates that the ICR does not move downward rapidly at the onset of flexion which contributes to maintaining knee stability during weight bearing. If the ICR were to shift downward too quickly, the amputee would have difficulty controlling the knee under load even with a small unintentional flexion.
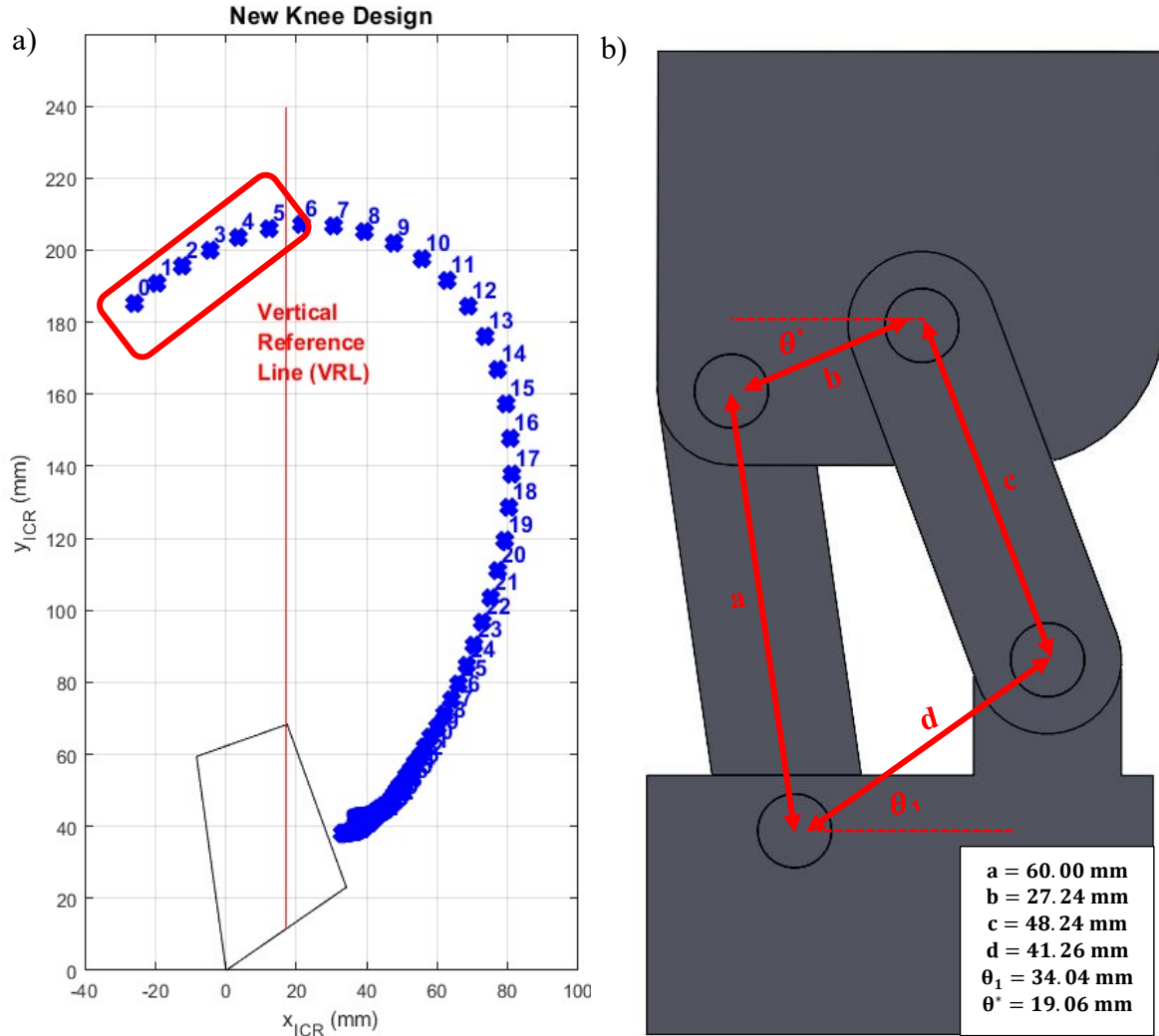
Figure 19: (a) ICR Trajectory of New Knee Design, (b) Initial 3D CAD with 2D Representation of 4 Bars

Furthermore, stability during flexion and extension was examined by evaluating the ICR position relative to the load line at heel contact and push-off. As shown in Figure 20, the ICR was found posterior to the load line at heel contact, exhibiting a negative x/y ratio, as well as, anterior to the load line at push-off, where the x/y ratio approached zero. These results indicate that no active hip moment is required during heel contact (hip relaxation) and that only a minimal moment is needed during the swing phase, confirming stable and efficient knee behavior throughout the gait cycle.
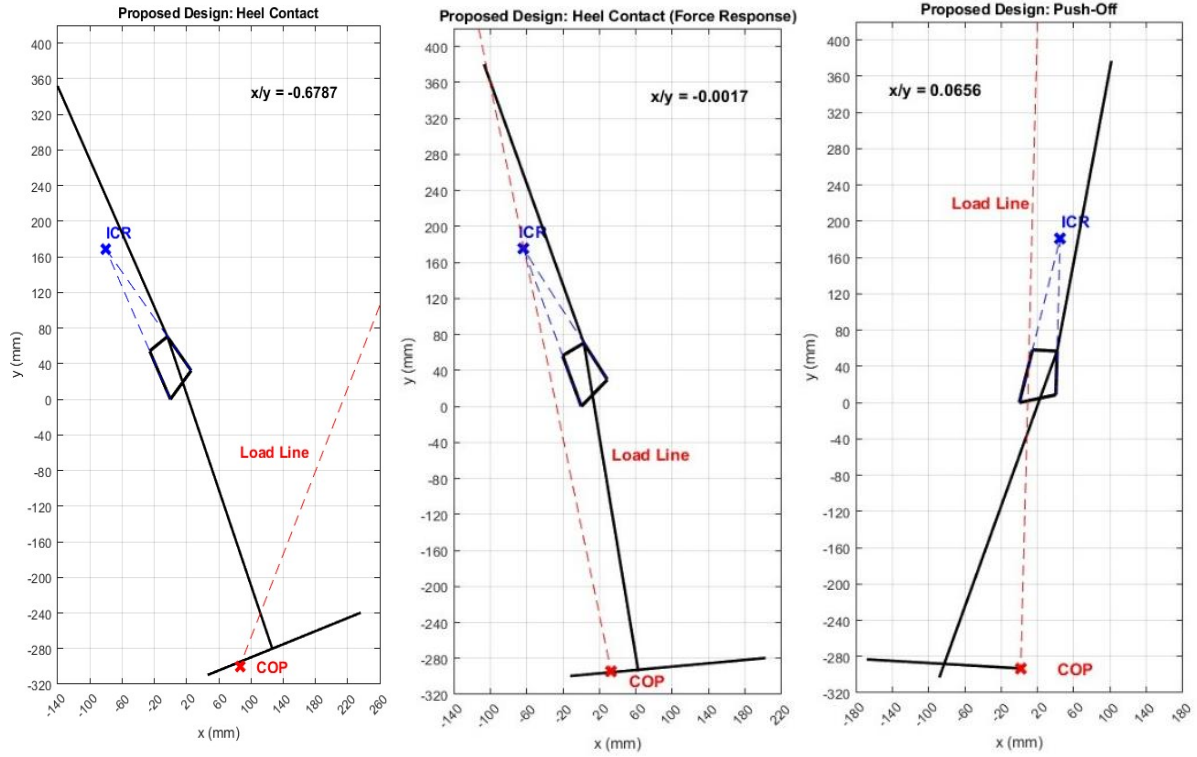
Figure 20: Stability Verification for New Design

3.2. Structural Study (ANSYS) Results

3.2.1. Validation of Constraints

A 1000 N force was applied in the z-direction, perpendicular to the top surface. All contacts were set to "No Separation" (sliding allowed without gaps) except for three bonded interfaces: pin O_A–base hole, pin O_A–central bar hole, and pin A–central bar hole. These bonded definitions were chosen because they provided results consistent with the analytical equilibrium calculations obtained from Eq. 15-19 derived from the Free Body Diagrams shown in Figure 21.
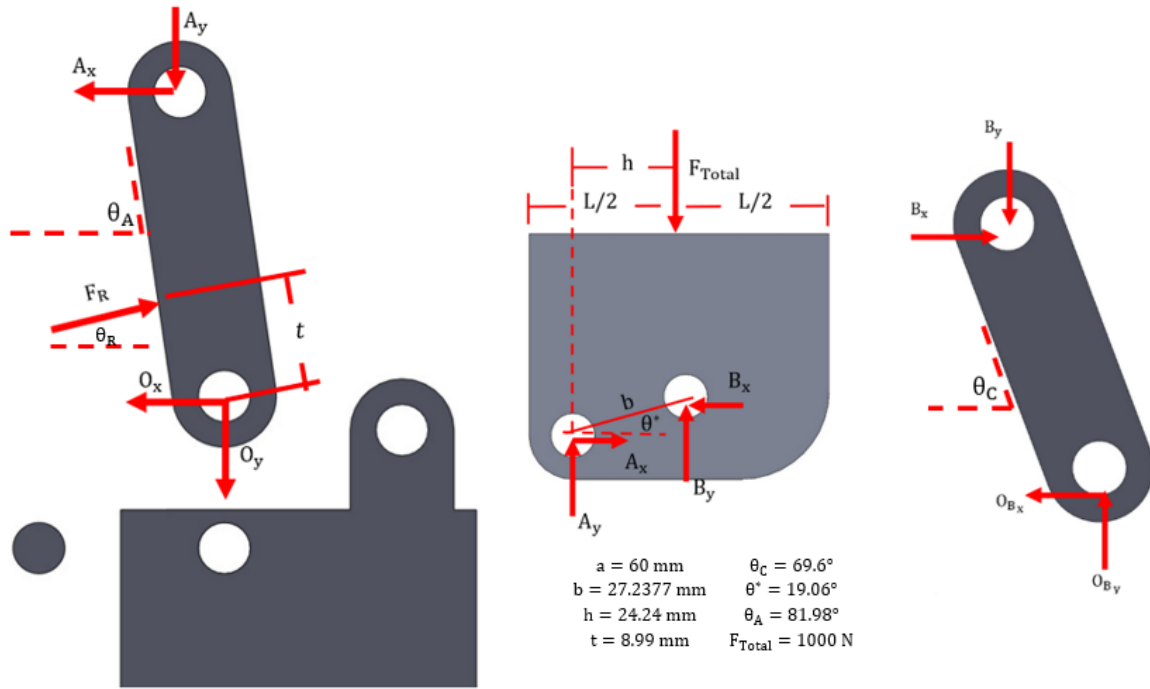
Figure 21: Free Body Diagrams for Top, Central Bar, and Side Bar

$$\sum M_A = F_B \sin\theta_C (b\cos\theta^*) + F_B \cos\theta_C (b\sin\theta^*) - F_{Total} \cdot h = 0 \dots\dots\dots\dots\dots (15)$$

$$\sum F_y = A_y + B_y - F_{Total} = 0 \dots\dots\dots\dots (16)$$

$$\sum M_{O_A} = -A_x (a\sin\theta_A) + A_y (a\cos\theta_A) - F_R t = 0 \dots\dots\dots (17)$$

$$\sum F_x = A_x - O_{A_x} - F_R \cos\theta_R = 0 \dots\dots\dots\dots (18)$$

$$\sum F_y = -A_y + O_{A_y} + F_R \sin\theta_R = 0 \dots\dots\dots\dots (19)$$

After obtaining the reaction forces at the joints, these forces were resolved into their horizontal and vertical components for the central bar to construct the corresponding shear and moment diagrams (see Figure 22).
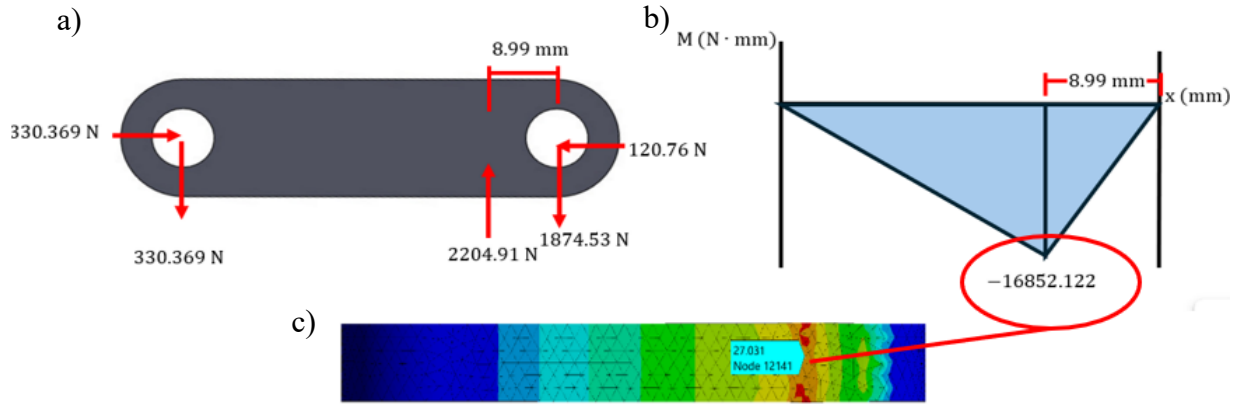
Figure 22: Moment Diagram and Critical Stress from Central Bar
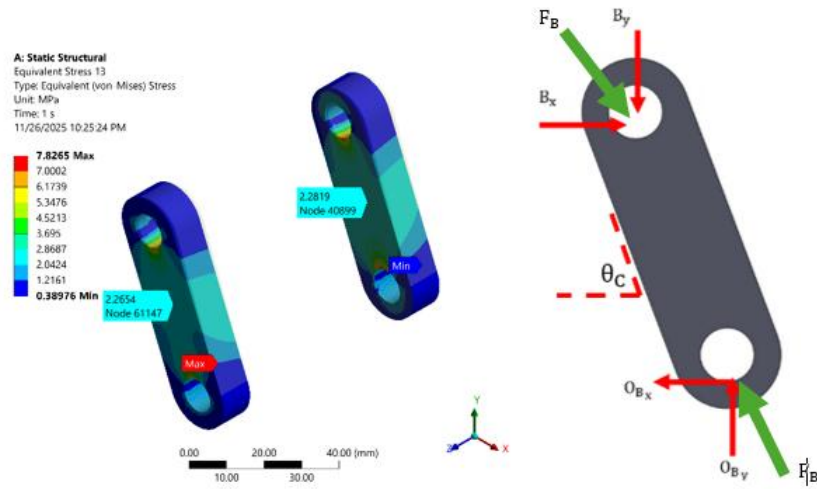
Figure 23: Stress Distribution from Side Bars

Analytical calculations predicted a bending stress of 25.27 MPa, while FEA estimated 27.031 MPa, yielding a 6.97% error. The stress distribution in Figures 22b and 22c agrees with the analytical moment diagram, with steeper regions indicating higher gradients and gentler regions indicating lower ones. The side bars also behaved as expected for weightless links under axial loading (Figure 23), having an error of only 0.247%.

3.2.2. ISO 10328 Loading Conditions

After achieving convergence, a 1.2 mm mesh was selected for further analysis (Figure 24b and 25b). For Condition 1 (Heel Contact), the minimum safety factor was 0.197, located in the posterior region of the central bar while for Condition 2, the lowest safety factor was 0.227 (Figure 26). Because this value is far below the target SF $\geq$ 1.25, a redesign was necessary. To guide the modifications, stress plots for each component were examined to identify critical regions. Material

was added strategically in these areas to ensure the redesigned components satisfy the required safety factor.
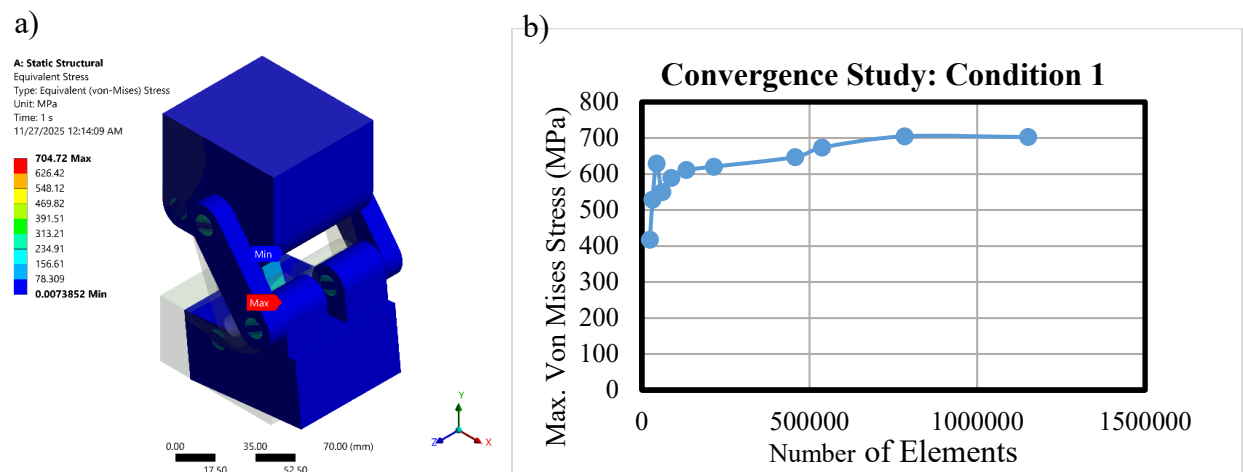

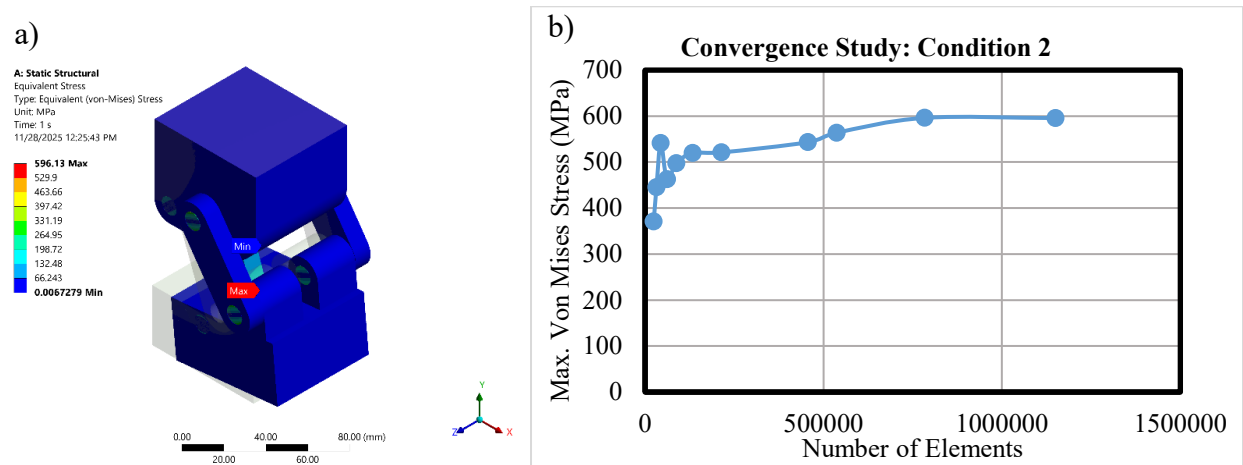Figure 24: Condition 1. a) Von Mises Stress Plot with 1.2 mm mesh, b) Convergence Study

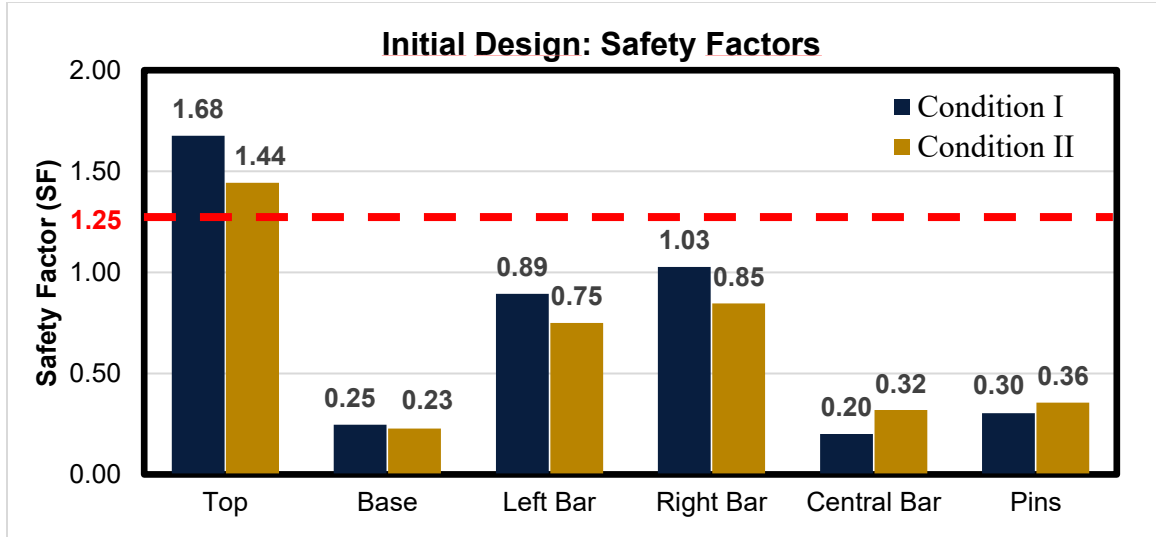Figure 25: Condition 1. a) Von Mises Stress Plot with 1.2 mm mesh, b) Convergence Study

Figure 26: Individual Safety Factors for Condition 1 (Initial Design)

Stress distributions for Condition 1 and Condition 2 were similar, so results from Condition 1 were considered to examine the stress plots for each component as follows:

- **Pins and holes in the bars, top, and base:** High stresses were concentrated around the holes, suggesting increase bar thickness or enlarge the pin and hole diameter to reduce bearing stresses (See Figure 27a-27f).

- **Central bar:** Elevated bending stress indicated the need to increase its width or thickness to raise the area moment of inertia. Another option was to increase the height of the stopper to decrease the reaction force F_R by increasing t (see Eq. 17 solved for F_R) and also the stress concentration on the sides from contact area (See Figure 27b).

- **Base:** Stress concentrations were observed at the end in contact with the central bar, requiring reinforcement in that region (See Figure 27a)
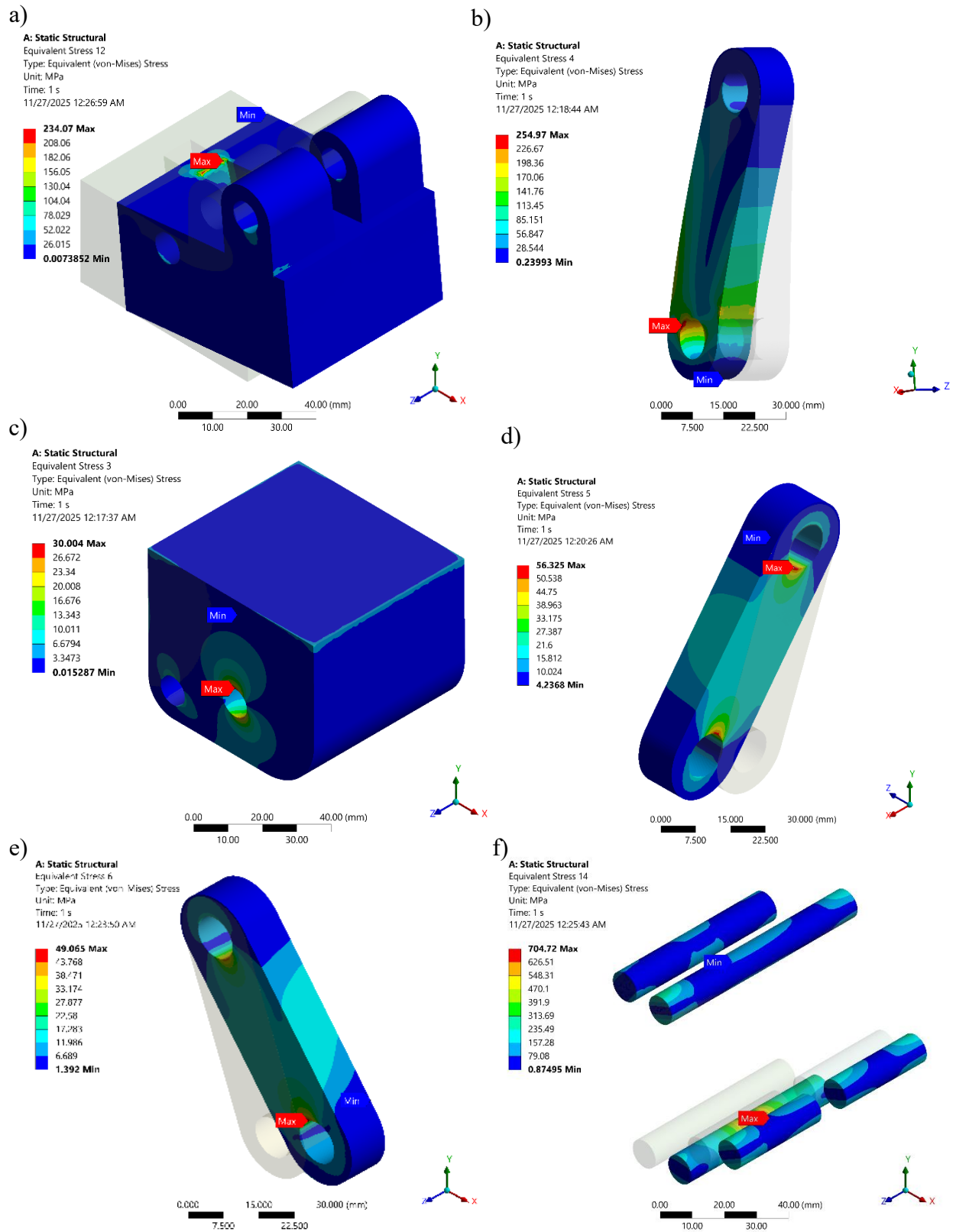
Figure 27: Condition 1. Stress Plots from a) Base, b) Central Bar, c) Top, d) Side Bar 1, e) Side Bar 2, f) Pins

After reinforcing the high-stress regions and removing material from the central portion of the top—since this area no longer acted as a flexion stopper—the redesigned model showed substantial performance improvements. As observed in Figures 28a and 28b, the maximum stresses decreased by 81.1% under Condition 1 and 73.7% under Condition 2. Additionally, comparing Figures 26 and 29 reveals a consistent increase in safety factors across all components. The minimum safety factor after redesign was 1.26 at the central bar, satisfying the requirement of SF ≥ 1.25.
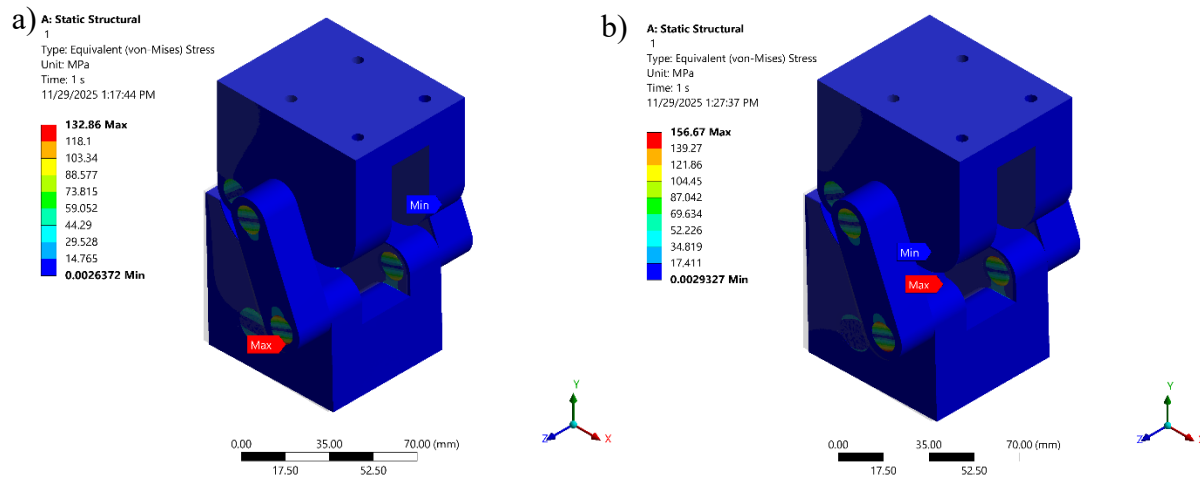

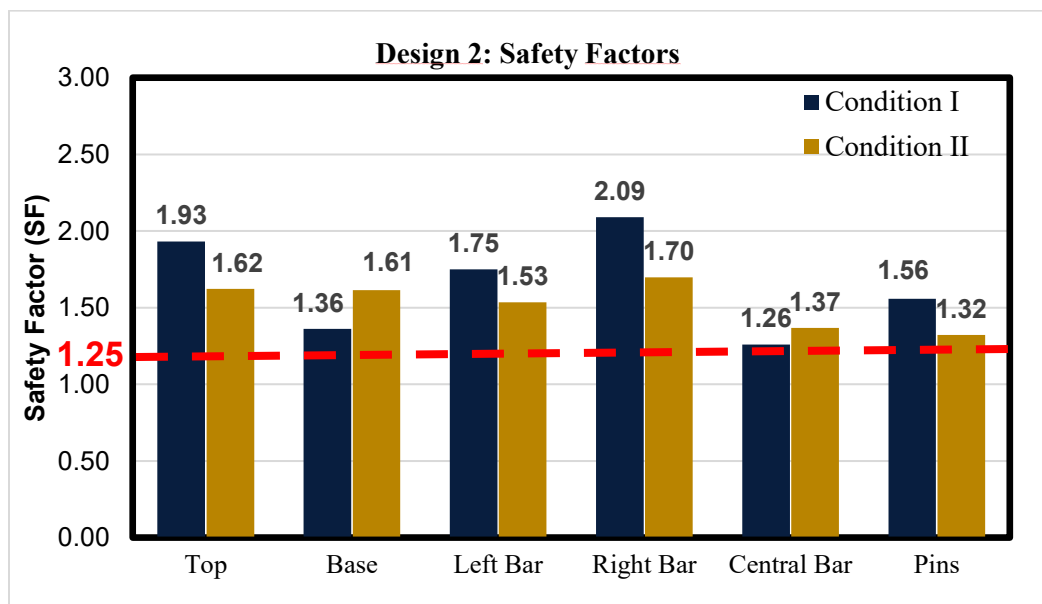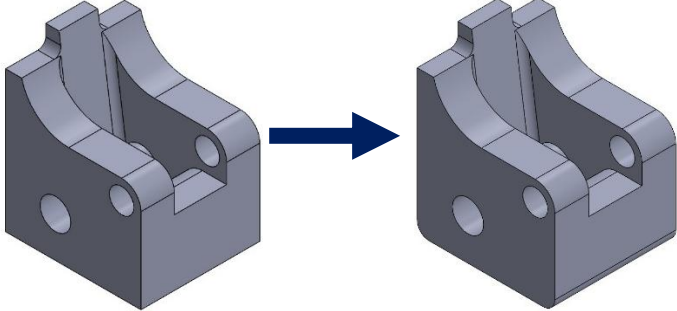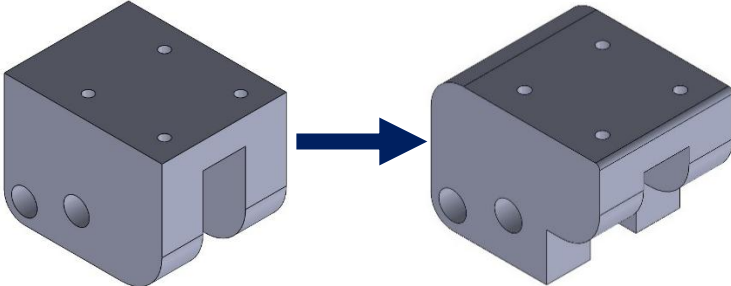Figure 28: Assembly Stress Plots. a) Condition 1 & b) Condition 2

Figure 29: Safety Factors after Material Addition (Design 2)

However, several regions showed very high safety factors (blue regions), indicating slight over-design. This suggests that further mass reduction is feasible. Nonetheless, any additional removal of material must consider the trade-off between mass, available space to avoid inter-component collisions, and the stress levels around the pin holes, which remain critical design constraints. This is particularly important given that commercial options—such as the 680 g Remotion Knee, made from injected plastic [35]—achieve significantly lower weight.
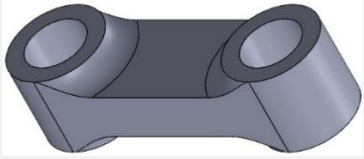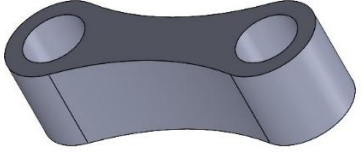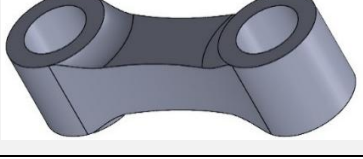
3.2.3. Topology Optimization

Less critical regions underwent material reduction. Initial modifications focused on the top and base, which were the least structurally constrained (See Table 10).

Table 10: Topology Optimization for Top and Base

CAD Design (Before → After)	Description
	• Bottom fillets added to cut material.
	• Front and rear fillets to reduce material and refine the knee-like profile. • Removed front-section material for additional weight reduction. • Removed middle-section material since it was not required as a stopper; this also required splitting the front top pin into two, further reducing weight.

Beyond these general modifications, several iterations were performed on the side bars. The most critical regions were the pin holes, so adjustments were limited to changes in the cross-sectional area (See Table 11).

Table 11: Side Bars Re-Design

CAD Design (Before → After)	Description
	• Mass = 33.84 g • $SF_{min-Assembly} = 1.2489$
	• Mass = 33.87 g • $SF_{min-Assembly} = 1.2516$
	• Mass = 29.42 g • $SF_{min-Assembly} = 1.2472$

After evaluating the first two iterations (reduced width and thickness), both changes were combined in a final iteration that maintained a minimum safety factor near 1.25 while achieving a 5.64% weight reduction, as summarized in Tables 10–11 and shown in Figure 30.
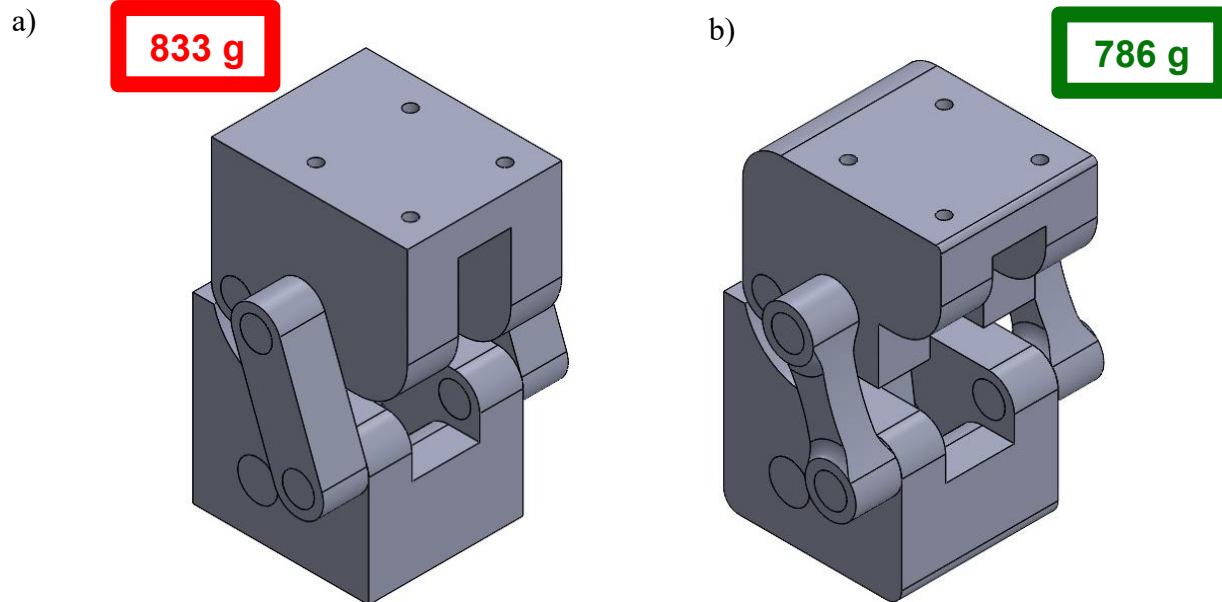
a)

833 g

b)

786 g

Figure 30: Design Optimization: a) Design 2, b) Final Design

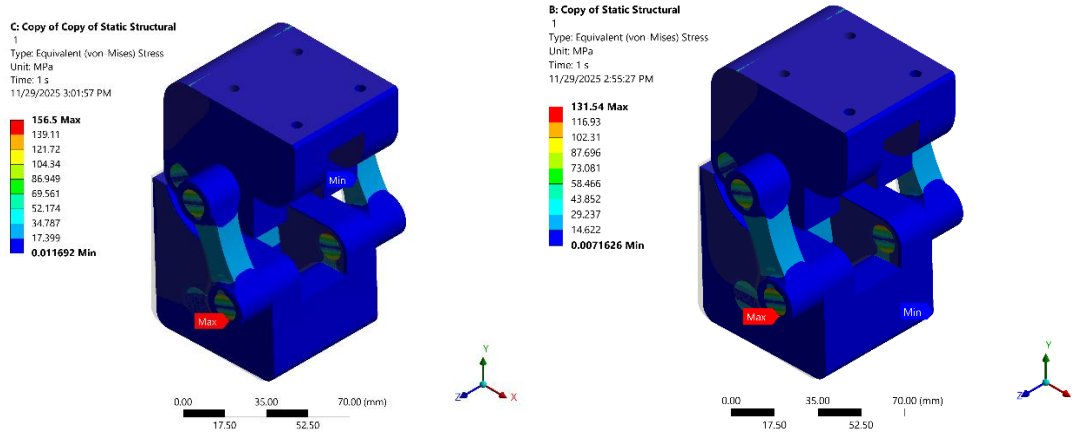Figure 31: a) Design 2, b) Final Design
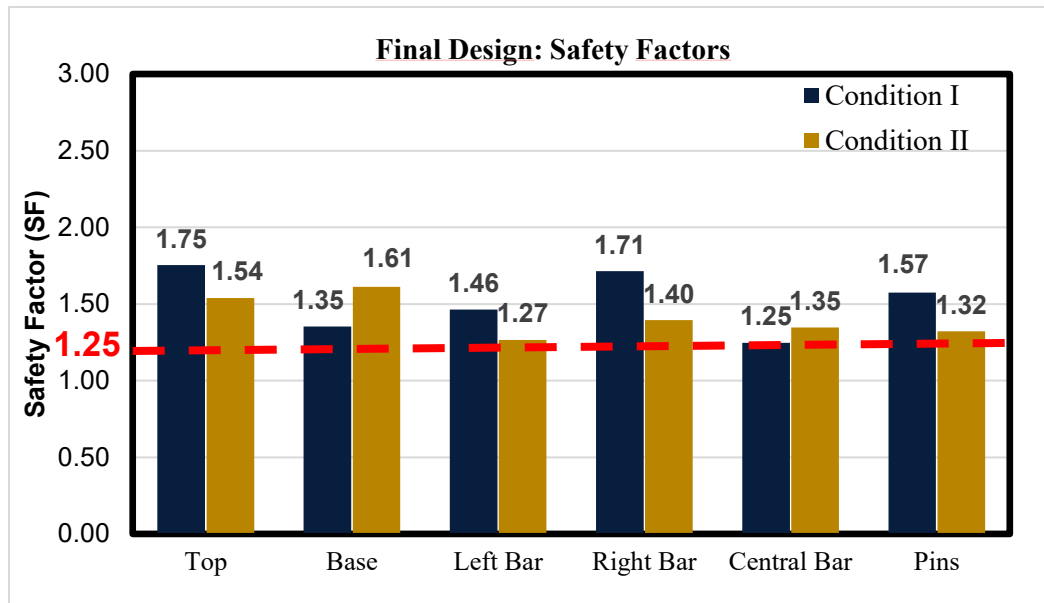

Figure 32: Safety Factors after Material Removal (Final Design)

Final safety-factor checks confirmed SF_{min} = 1.25 with a simultaneous weight reduction. Although the prosthesis remains 106 g heavier than the Remotion Knee, the redesign maintains $SF_{min} \geq 1.25$ with PLA components and is still 12.2% lighter than comparable commercial joints (Table 12).

Table 12: Comparison of Weights between Knees from the Market and Final Design

Knee	Weight (g) [34] [35]	Weight Reduction (%)
Rheo Knee (K2)	1630	51.8%
Ottobock 3R62 (K1,K2)	955	17.7%
Ottobock Kenevo (K1,K2)	916	14.2%
Ottobock 3R92 (K2,K3)	895	12.2%
Ottobock 3R80 (K3,K4)	1240	36.6%
Ottobock C-leg (K2, K3,K4)	1250	37.1%
Orion 3	1500	47.6%

3.3. Prototype and post-processing

Once the parts were printed and their support removed, they were coated with a thin layer of epoxy resin and allowed to cure for approximately 24 hours at room temperature. This allows for a protective outer layer to form, priming the part for sanding without the removal of excess material and preserving dimensional accuracy. Additionally, the epoxy can act as a thermal barrier, preventing the PLA from softening due to friction from sanding, while simultaneously increasing the overall surface hardness and mechanical strength of the printed components. After curing, the parts were wet sanded with different grits used in progression, starting at 150 grit and finishing at 600 grit. Once the sanding of the part was completed, gap filling was done with epoxy for smaller holes and Bondo/autobody filler for larger gaps. The optional step of adding an acrylic primer for plastics designed to adhere to paints was not done for this project but should still be noticed as a step that can be done for the knee. Once sanding was completed, the art was sprayed by a UV-resistant acrylic clear coat to protect the epoxy surface from photodegradation, as prolonged UV exposure can cause epoxy resins to yellow and lose mechanical integrity over time.

4. Conclusion

This project sets out to design a prosthetic knee that could genuinely make a difference for above-the-knee amputees in underserved communities, where cost, durability, and accessibility often determine whether someone can walk comfortably again. By following a structured and iterative engineering process, the team developed a four-bar linkage knee that meets the original problem statement while staying mindful of real-world constraints such as local manufacturing capabilities, environmental conditions, and long-term usability.

Through kinematic modeling, Differential Evolution optimization, material testing, and detailed structural analysis, the project created a design that performs reliably under the demands of daily gait. The optimization process proved especially meaningful, reducing kinematic error by 39% compared to Genetic Algorithms and producing a smoother, more natural ICR trajectory. Moreover, material testing following ASTM D695 strengthened the accuracy of the simulations, and repeated design iterations improved the minimum safety factor from below 0.25 in the early prototype to 1.26 in the final version, successfully meeting ISO 10328 requirements. Similarly, our final design achieved a flexion angle of 93.37°, which falls right within the ideal 90-100° range needed for sitting, squatting, and everyday activities. This is important since it ensures the knee feels natural and functional for users, allowing them to perform essential movements comfortably and safely. Weight was reduced to 786g which is 12.2% lighter than similar mechanical knees, and the final cost remained at $98.09 when adapters are reused, making it a realistic option for low-income regions.

Beyond the numbers, this project shows that thoughtful engineering can bridge gaps in healthcare access. Using FDM 3D printing, standard hardware, and locally manufacturable components means clinics in resource-limited areas could realistically build, repair, and distribute this knee without relying on expensive industrial equipment. Furthermore, environmentally, additive manufacturing also helps reduce waste and makes on-demand production feasible.

Looking ahead, future work should explore fatigue and cyclic loading tests, real-user gait trials, and the transition to reinforced polymers or hybrid materials for longer lifespan. Additional refinements could also focus on manufacturability guidelines, modularity, and fit customization. Overall, this work demonstrates that a low-cost, safe, and functional prosthetic knee is not only

technically achievable but can also play a meaningful role in improving mobility and quality of life for people in developing communities.

Acknowledgement

References

[1] World Health Organization (WHO), "Global report on health equity for persons with disabilities," Geneva, Dec. 2022. Accessed: Feb. 19, 2025. [Online]. Available: https://digitallibrary.un.org/record/3998942?ln=es&v=pdf

[2] B. Yuan, H. Dong, S. Gu, S. Xiao, and F. Song, "The global burden of traumatic amputation in 204 countries and territories," *Frontiers in Public Health*, vol. 11, Oct. 2023, doi: https://doi.org/10.3389/fpubh.2023.1258853.

[3] D. Manodritto, "The ISO 10328:2006 static testing and finite element analysis of the ICRC prosthetic knee for use in low-income countries," STAX, 2021. https://stax.strath.ac.uk/concern/theses/vq27zn538 (accessed Feb. 20, 2025).

[4] B. T. Amador, R. R. Torrealba, M. Rojas, J. Cappelletto, and C. M. Müller-Karger, "METODOLOGÍA PARA DIMENSIONAMIENTO DE MECANISMO POLICÉNTRICO DE RODILLA UTILIZANDO ANÁLISIS DE MARCHA Y ALGORITMOS GENÉTICOS," Revista Ingeniería Biomédica, vol. 6, no. 11, pp. 30–45, 2025, Accessed: Feb. 20, 2025. [Online]. Available:http://www.scielo.org.co/scielo.php?script=sci_arttext&pid=S1909-97622012000100004

[5] B. Yuan, H. Dong, S. Gu, S. Xiao, and F. Song, "The global burden of traumatic amputation in 204 countries and territories," *Frontiers in Public Health*, vol. 11, Oct. 2023, doi: https://doi.org/10.3389/fpubh.2023.1258853.

[6] Phoengsongkhro, Santiphap, et al. "Development of Four-Bar Polycentric Knee Joint with Stance-Phase Knee Flexion." *Nature News*, Nature Publishing Group, 20 Dec. 2023, www.nature.com/articles/s41598-023-49879-4.

[7] C. W. Radcliffe, "Four-bar linkage prosthetic knee mechanisms: Kinematics, alignment and prescription criteria," *Prosthetics and Orthotics International*, vol. 18, no. 3, pp. 159–173, Dec. 1994, doi: https://doi.org/10.3109/03093649409164401.

[8] S. Lapapong et al., "Finite element modeling and validation of a four-bar linkage prosthetic knee under static and cyclic strength tests," *Journal of Assistive Rehabilitative & Therapeutic Technologies*, vol. 2, no. 1, p. 23211, Jan. 2014, doi: 10.3402/jartt.v2.23211.

[9] S. R. Hamner, V. G. Narayan, and K. M. Donaldson, "Designing for Scale: Development of the ReMotion Knee for Global Emerging Markets," *Annals of Biomedical Engineering*, vol. 41, no. 9, pp. 1851–1859, Mar. 2013, doi: https://doi.org/10.1007/s10439-013-0792-8.

[10] D. Manodritto, "The ISO 10328:2006 Static Testing and Finite Element Analysis of the ICRC Prosthetic Knee for Use in Low Income Countries," *University of Strathclyde Department of Biomedical Engineering*, 2006.

[11] B. T. Amador, R. R. Torrealba, M. Rojas, J. Cappelletto, and C. M. Müller-Karger, "METODOLOGÍA PARA DIMENSIONAMIENTO DE MECANISMO POLICÉNTRICO DE RODILLA UTILIZANDO ANÁLISIS DE MARCHA Y ALGORITMOS GENÉTICOS," Revista Ingeniería Biomédica, vol. 6, no. 11, pp. 30–45, 2025, Accessed: Feb. 20, 2025. [Online]. Available: http://www.scielo.org.co/scielo.php?script=sci_arttext&pid=S1909-97622012000100004

[12] S. Ebrahimi and P. Payvandy, "Efficient constrained synthesis of path generating four-bar mechanisms based on the heuristic optimization algorithms," *Mechanism and Machine Theory*, vol. 85, pp. 189–204, Mar. 2015, doi: https://doi.org/10.1016/j.mechmachtheory.2014.11.021.

[13] International Organization for Standardization (ISO). *Prosthetics. Structural Testing of Lower-Limb Prostheses. Requirements and Test Methods*, 2016, https://doi.org/10.3403/30074527uhttps://doi.org/10.3403/30074527u.

[14] Blatchford. (n.d.). *Orion3 Prosthetic Knee.* https://www.blatchford.co.uk/products/orion3/

[15] https://www.cs.cmu.edu/~rapidproto/mechanisms/chpt5.html

[16]   C. Radcliffe, "Biomechanics of Knee Stability Control with Four-Bar Prosthetic Knees," 2003. Accessed: Mar. 30, 2025. [Online]. Available: https://rehabtech.com.au/techguide/pdf/kneeControl.pdf

[17]   Viladot, R., Ortesis y prótesis del aparato locomotor ©1994 Últ. Reimpr. 2005

[18]   B. T. Amador, R. R. Torrealba, M. Rojas, José Cappelletto, and C. M. Müller-Karger, "METHODOLOGY TO GAUGE A FOUR-BAR LINKAGE PROSTHETIC KNEE MECHANISM BASED ON GAIT ANALYSIS AND GENETIC ALGORITHMS," *Revista Ingeniería Biomédica*, vol. 6, no. 11, pp. 30–45, Jun. 2012.

[19]   Gard, S., Childress, D. y Uellendahi, J. The Influence of four-bar linkage knees on prosthetic swing-phase floor clearance. *Journal of Prosthetics and Orthotics*, 8(2), 34-40, 1996.

[20]   C. W. Radcliffe, "Four-bar linkage prosthetic knee mechanisms: Kinematics, alignment and prescription criteria," *Prosthetics and Orthotics International*, vol. 18, no. 3, pp. 159–173, Dec. 1994, doi: https://doi.org/10.3109/03093649409164401.

[21]   S. Ebrahimi and P. Payvandy, "Efficient constrained synthesis of path generating four-bar mechanisms based on the heuristic optimization algorithms," Mechanism and Machine Theory, vol. 85, pp. 189–204, Mar. 2015, doi: https://doi.org/10.1016/j.mechmachtheory.2014.11.021.

[22]   K. Rajwar, K. Deep, and S. Das, "An exhaustive review of the metaheuristic algorithms for search and optimization: taxonomy, applications, and open challenges," Artificial Intelligence Review, Apr. 2023, doi: https://doi.org/10.1007/s10462-023-10470-y.

[23]   M. Horak, "Chemical resistance of 3D printing materials | Prusament," *prusament.com*, Oct. 18, 2021. [Online]. Available: https://prusament.com/chemical-resistance-of-3d-printing-materials/

[24]   "Manufacturing Materials | Polymers, Resins, Rubber & Metals," *Vexmatech.com*, 2025. [Online]. Available: https://vexmatech.com/material

[25]   MatWeb, "PA66-GF30, Glass Fiber Reinforced Nylon 66." [Online]. Available: http://www.matweb.com/search/DataSheet.aspx?MatGUID=1c8e2b1e08c84f4f9b3c5e8e8d7b4f77

[26]   https://all3dp.com/2/3d-printer-material-cost-the-real-cost-of-3d-printing-materials/

[27]   CNCLATHING, "Metal strength chart – mechanical properties chart of different metal grades and alloys," *CNCLATHING.com*, Mar. 27, 2020. [Online]. Available: https://www.cnclathing.com/guide/metal-strength-chart-mechanical-properties-chart-of-different-metal-grades-and-alloys-cnclathing

[28]   "Galvanic Corrosion – SSINA," *Specialty Steel Industry of North America (SSINA)*. [Online]. Available: https://www.ssina.com/education/corrosion/galvanic-corrosion/

[29]   "4-Hole Male Pyramid Adapter TI," *Össur*, [Online]. Available: https://www.ossur.com/en-as/prosthetics/adapters/4-hole-male-pyramid-adapter-ti

[30]   "Steel vs. Titanium – Strength, Properties, and Uses," *ThomasNet*, Jun. 16, 2025. [Online]. Available: https://www.thomasnet.com/articles/metals-metal-products/steel-vs-titanium-strength-properties-and-uses/

[31]   "Nuts–Hex A2," MonsterBolts.com. [Online]. Available: https://monsterbolts.com/products/nuts-hex-a2?srsltid=AfmBOoqZnAWtXpsGRflULbrtYMly_nqLrIr8rzA5NmJjqXCu5sczsV7a.

[32]   https://store.astm.org/d0695-23.html

[33]   Lugo, L. (2006). Semiología del aparato locomotor de la persona normal. En Duque, L. y Rubio, H.(Eds.). Semiología médica integral(pp. 369-394). Medellín: Universidad de Antioquia.

[34]   ISO 10328. (2006). Prosthetics – Structural testing of lower-limb prostheses – Requirements and test methods. First edition.

[35]   https://cargocollective.com/futurehealth/ReMotion-Knee